Sea ice sources of sea salt aerosols in polar regions

Jiayue Huang

A dissertation

submitted in partial fulfillment of the

requirements for the degree of

Doctor of Philosophy

University of Washington

2018

Reading Committee:

Lyatt Jaeglé, Chair

Becky Alexander

Joel Thornton

Program Authorized to Offer Degree:

Department of Atmospheric Sciences

University of Washington

Abstract

Sea ice sources of sea salt aerosols in polar regions

Jiayue Huang

Chair of the Supervisory Committee:

Professor Lyatt Jaeglé

Department of Atmospheric Sciences

Blowing briny snow and frost flowers have been suggested as important sources of sea salt aerosols (SSA) over sea ice covered regions, where they can affect radiation, cloud formation, and boundary layer chemistry. During polar spring, observations show periodic near total ozone depletion events (ODEs) in the boundary layer. These ODEs are initiated by the release of reactive bromine gases, however the origin of the reactive bromine has been subject to debate. In particular, saline surface snow, blowing snow SSA and frost flowers SSA have been proposed as potential sources releasing bromine. My Ph.D. research aims to provide new constraints on blowing snow and frost flower sources of SSA and assess their impact on tropospheric chemistry by using satellite observations together with a chemical transport model (CTM).

In the first part of my Ph.D. project (Chapter 2), I interpreted observations of aerosol extinction coefficients from the Cloud-Aerosol Lidar with Orthogonal Polarization (CALIOP) instrument onboard the Cloud-Aerosol Lidar and Intrared Pathfinder Satellite Observations (CALIPSO)

with the GEOS-Chem CTM to evaluate the role of sea ice sources of SSA in the Arctic and Antarctic boundary layer. I find that the inclusion of blowing snow SSA emissions is necessary for the GEOS-Chem model to reproduce the CALIOP aerosol extinctions over sea ice regions during cold months, but that frost flower SSA fail to do so. Using the CALIOP aerosol extinction coefficients, I derived monthly-varying surface snow salinities, which further improves the performance of the blowing snow GEOS-Chem simulation.

In the second part of my Ph.D. project (Chapter 3), I implemented bromine release from SSA generated via blowing snow events, and evaluated the model against tropospheric BrO columns retrieved from the Second Global Ozone Monitoring Experiment (GOME-2) onboard the MetOp-A satellite and the Ozone Monitoring Instrument (OMI) onboard the Aura satellite, as well as in-situ observations of surface ozone over the Arctic. I find that bromine release from blowing snow SSA in GEOS-Chem allows the model to capture the timing and locations of the observed bromine explosion events and some of the observed ODEs in the springtime Arctic. I estimated that the halogen chemistry from blowing snow SSA increases the Br_y abundance by a factor of 2.6 and decreases the O_3 abundance by 10% in the Arctic lower troposphere (0–2 km) during spring (March–May).

TABLE OF CONTENTS

LIST OF FIGURES

LIST OF TABLES

ACKNOWLEDGEMENTS

I feel extremely fortunate and grateful to receive a lot of help and love from lots of you in my past five years in Seattle.

First, I would like to express my gratitude to my PhD advisor, Lyatt Jaeglé, for offering me the opportunities to conduct research and the guidance to help me learn and grow as a scientist. I am particularly grateful for Lyatt's patience, encouragement, extremely helpful guidance and full support throughout my PhD life here.

I would also like to thank my PhD committee: Professor Becky Alexander, Cecilia Bitz, Joel Thornton, and Ed Waddington, as well as Professor Steve Warren, for all the helpful and insightful comments, advice and discussions on my research topics. Becky and Joel offered a lot of help from the chemistry prospective. Cecilia, Steve and Ed helped me a lot in learning snow and ice. I would also like to thank NASA CALIPSO team and Harvard GEOS-Chem community for offering the great products and addressing my questions.

I am also deeply grateful to meet and be friends with the Jaeglé group members, especially Viral Shah. I would also like to thank Grads13 for all the support, helps and fun throughout the last 5 years, especially Qianjie who has been an awesome classmate and friend for a decade. I also feel extremely grateful to all my friends I met in Guangdong, Hampton and Seattle, who offered me enormous support and love, and helped me through all the ups and downs. I could not have made it through the Seattle drizzle without the fun and joy brought by each single one of you. A special thanks to Dr. Hongyu Liu and his family for the mentorship, and for always being supportive, encouraging and believing in me.

Finally, I would like to express my gratitude to my family: my parents and my brother for their unconditional love and support. Thank you for everything.

DEDICATION

To my family, for their endless love and support.

献给我最亲爱的父亲, 母亲, 哥哥

Chapter 1.

INTRODUCTION

1. 1 MOTIVATIONS AND SCIENTIFIC GOALS

Sea salt aerosols (SSA) are important for radiation, cloud formation, and boundary layer chemistry over polar regions. While large particles (>1 μm) dominate SSA total mass concentrations, the number concentrations of SSA are dominated by smaller particles, which can effectively scatter solar radiation (Quinn and Coffman, 1999), as well as change cloud albedo by acting as efficient cloud condensation nuclei (O'Dowd and Smith, 1993; Pierce and Adams, 2006). In addition, SSA can act as reservoir for chlorine and bromine, affecting the photochemical process in the marine boundary layer (Vogt et al. 1996). Once activated, these reactive chlorine and bromine which can lead to catalytic ozone loss (Fan and Jacob, 1992). Halogen release from SSA has been proposed as an explanation for the springtime bromine explosions and resulting ozone depletion events (ODEs) that are often observed at Arctic and Antarctic coastal sites and over sea ice (Wennberg, 1999; Nghiem et al., 2012). Reactive halogen release from SSA can also oxidize atmospheric mercury vapor transported to polar regions, and lead to increased mercury deposition to polar ecosystems (Lu et al., 2001).

The sources and spatial distributions of SSA over polar regions remain poorly constrained. Globally, SSA are mainly produced via breaking waves at the ocean surface (Lewis and Schwartz, 2004; de Leeuw et al., 2011). Model simulations that include only open ocean source of SSA predict summertime maxima of SSA when sea ice extent is smallest, which is in contrast with the observed wintertime maxima of SSA mass concentrations at polar surface sites (Quinn

et al., 2002; Weller et al. 2008). The open ocean source of SSA alone also fails to explain the increase in SSA deposition fluxes during glacial periods relative to interglacial periods in ice cores (Wolff et al., 2006; Fischer et al., 2007). In addition, wintertime SSA at polar surface sites have a low sulfate-to-sodium ratio relative to bulk sea water, suggesting a sea ice source of SSA (Rankin et al., 2000; Hara et al., 2012). To explain these observed inconsistencies, studies have proposed that SSA can be produced over sea ice surfaces via wind lifting of saline snow particles (Yang et al. 2008) or frost flower crystals (Rankin 2003, Wolff et al., 2003).

In my M.S. project (Huang and Jaeglé, 2017, "Wintertime enhancements of sea salt aerosol in polar regions consistent with a sea ice source from blowing snow", published in Atmospheric Chemistry and Physics), I implemented both blowing snow and frost flower SSA emissions into the GEOS-Chem chemical transport model and found that the blowing snow source was necessary to explain wintertime SSA mass concentration observations at several polar sites. The blowing snow emission is a function of wind speed, humidity, temperature, surface snow salinity, snow age (Yang et al., 2008). In particular, the blowing snow emission has a near-linear dependence on the surface snow salinity. I made simplifying assumptions for the surface snow salinity, the age of snow and number of particles produced per snowflake. These assumptions are poorly constrained based on sparse measurements of snow salinity on sea ice and SSA mass concentrations.

The scientific goals of my Ph.D. project were 1) to further evaluate the relative contributions and spatial distributions of blowing snow and frost flower SSA over polar region using satellite observations, and 2) to understand the role of blowing snow SSA in bromine explosions and ODEs. In my work, I use space-borne observations of aerosol extinction coefficients from the Cloud-Aerosol Lidar with Orthogonal Polarization (CALIOP) instrument onboard the Cloud-

Aerosol Lidar and Intrared Pathfinder Satellite Observations (CALIPSO) satellite to constrain blowing snow and frost flower SSA emissions over polar regions (Chapter 2); and I use tropospheric BrO columns from the Second Global Ozone Monitoring Experiment (GOME-2) and the Ozone Monitoring Instrument (OMI), as well as Arctic in-situ surface ozone observations to evaluate the role of SSA on Arctic springtime photochemistry (Chapter 3). The first part of my Ph.D. thesis (Chapter 2) is under review in Atmospheric Chemistry and Physics (Huang et al., 2018). The second part of my thesis (Chapter 3) is in preparation for submission for publication in the near future.

1. 2 BACKGROUND

1.2.1 Sea ice sources of SSA

Blowing snow events are often observed over snow covered sea ice regions (Nishimura and Nemoto, 2005; Savelyev et al., 2006). Salty surface snow particles on sea ice can be lifted by strong winds above ~ 7 m s^{-1} (Fig 1.1). Once lifted, these snow particles can be sublimated in the presence of low humidity, and produce SSA (Yang et al. 2008). Snow on sea ice becomes salty via upward migration of brine from the sea ice to the snow surface, incorporation of frost flowers, as well as SSA deposition from the adjacent open ocean (Domine et al., 2004). Yang et al. (2008) developed an emission scheme to calculate the SSA production via blowing snow events on sea ice. This blowing snow SSA scheme is a function of surface wind speed, surface snow salinity, snow age, relative humidity, and temperature. We implemented this blowing snow emission scheme in the GEOS-Chem chemical transport model (Huang and Jaeglé, 2017) and found that the blowing snow SSA emission is largest over sea ice regions in east of Greenland,

the central Arctic, Beaufort Sea, and the Ross and Weddell seas where strong winds often occur. In addition with this blowing snow SSA source, the model was able to reproduce the observed seasonal variation of SSA mass concentrations at five polar sites. Surface snow salinity is critical for estimates of the magnitude of blowing snow SSA emissions. With limited observations of surface snow salinity, however, the seasonal and spatial (multi-year sea ice versus first year sea ice) variations of the surface snow salinity are very uncertain.

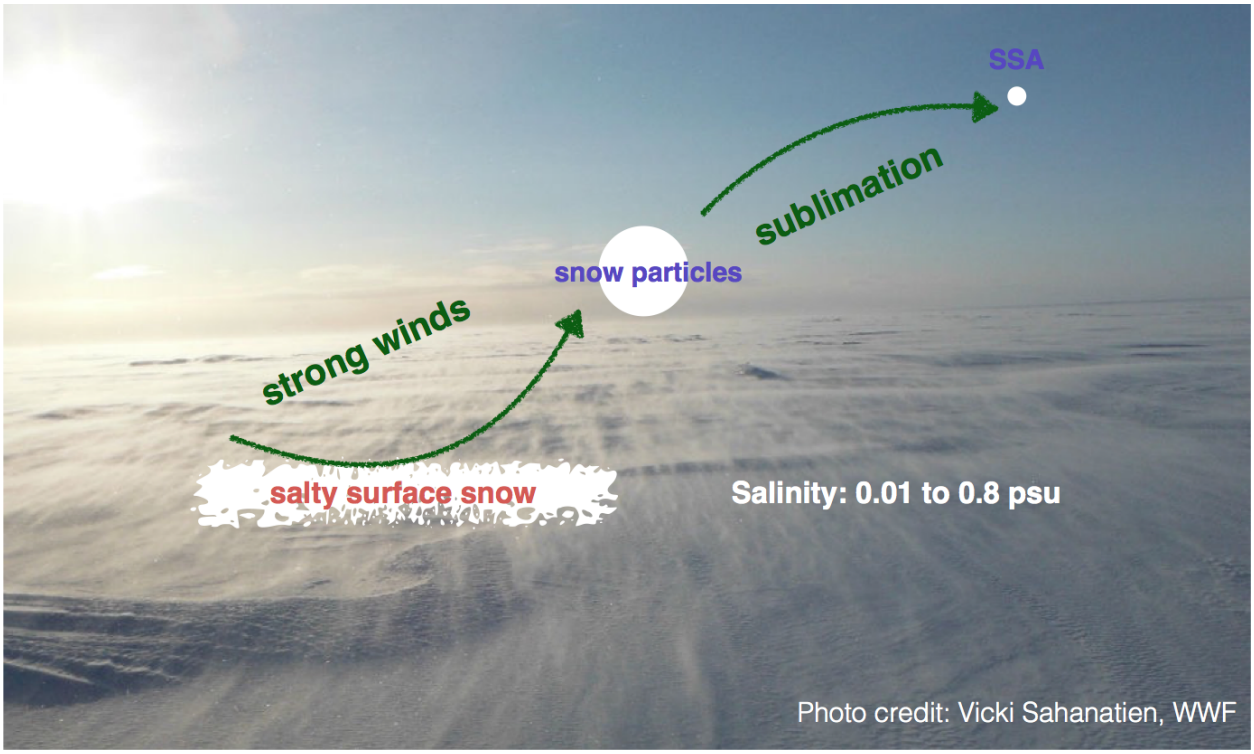

Figure 1.1 A schematic diagram of SSA production via a blowing snow event. Photo credit: Vicki Sahanatien, WWF.

The other proposed source of polar SSA is frost flowers, which are very salty ice crystals (>100 psu) that usually form on the newly frozen and young sea ice under cold ambient air temperature (<about -20^{o}C) (Martin et al., 1995; Kaleschke et al., 2004; Domine et al., 2005; Roscoe et al.,

2011). Frost flowers wick up brine from sea ice and can be lifted by even mild winds to produce SSA particles (Figure 1.2) (Rankin et al. 2000; Domine et al., 2004; Xu et al. 2013 and references therein). The role of frost flowers as a source of SSA has been debated. Some studies have shown that strong winds inhibit frost flower formation and bury existing frost flowers with snow (Perovich and Richeter-Menge, 1994; Rankin et al., 2000), while field experiments show that frost flowers are difficult to break (Domine et al., 2005; Alvarez-Avilez et al., 2008) and no breakage of frost flowers are observed in winds up to 6 m s^{-1} (Obbard et al. 2009). In addition, laboratory experiments show that evaporating frost flowers form a cohesive chunk of salt (Yang et al. 2017), and it produces no aerosol when exposed to large wind speeds (12 m/s) (Roscoe et al. 2011), making frost flower unlikely to be a direct source of SSA.

Xu et al. (2013) developed a parameterization of SSA production from frost flowers based on the potential frost flower (PFF) coverage derived by Kaleschke et al. (2004). With this frost flower SSA source implemented in the GEOS-Chem model (Huang and Jaeglé, 2017), we found that the derived frost flower emissions are strongest over the Canadian Arctic Archipelago, coastal regions of Siberia, and off the Ross and Ronne ice shelves where open leads and cold air temperature are co-located. However, we found that frost flower SSA could not reproduce the concentrations and variability of surface observations of SSA.

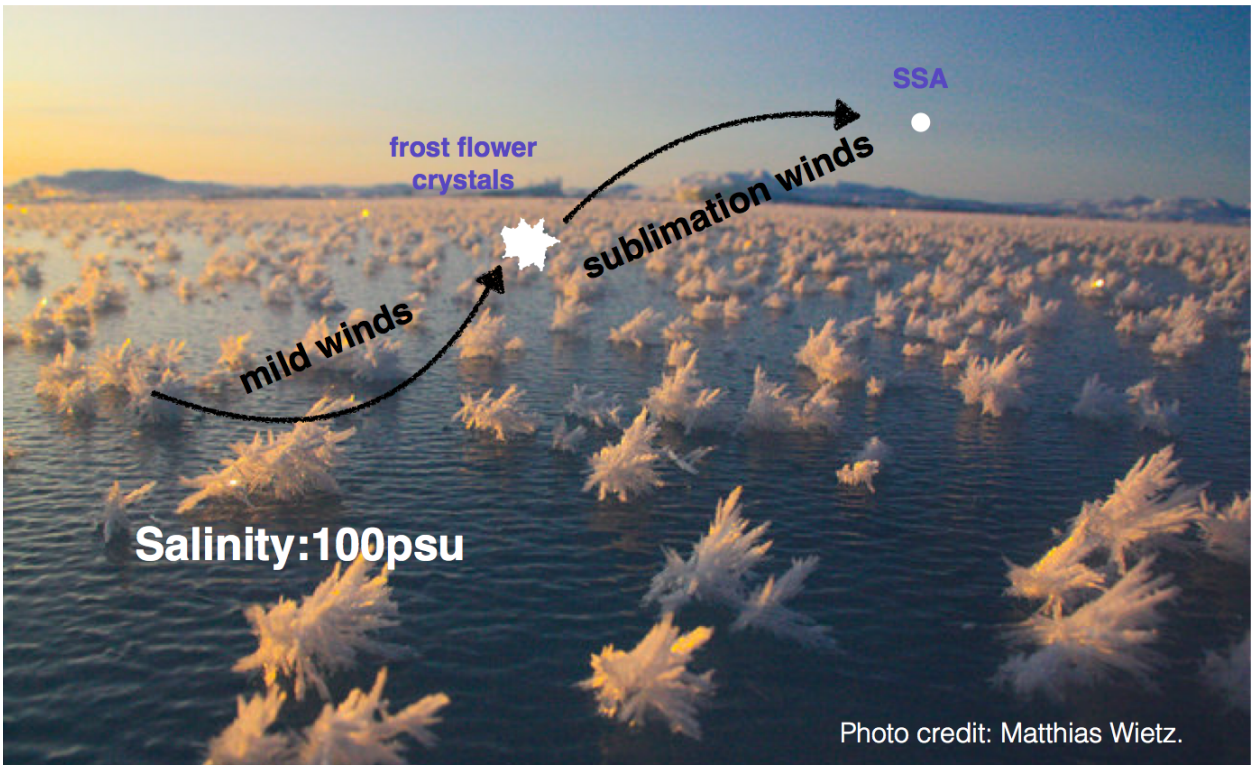

Figure 1.2 A schematic diagram of SSA production via frost flowers. Photo credit: Matthias Wietz.

1.2.2. Ozone depletion events

Surface ozone depletion events (ODEs) are first introduced by Oltman (1981) in which they found surface O_3 were often depleted to near zero during spring at Barrow, Alaska. Tarasick and Bottenheim (2002) examine the historical ozonesonde records and found that surface ODEs mostly occur during March-May over the Arctic and during September-November over the Antarctic, although the frequency of ODEs varies with different locations.

Barrie et al. (1988) found the observed springtime surface O_3 are anti-correlated with high aerosol bromine at Alert, Canada, and proposed that ODEs are associated with production of

aerosol Br and gaseous HBr in the boundary layer in presence of sunlight at polar sunrise. In particular, Barrie et al. (1988) proposed the following chain reactions that leads to ODEs:

$$CHBr_3 + hv \rightarrow Br + CHBr_2 \quad (1)$$

$$HBr + OH \rightarrow Br + H_2O \quad (2)$$

$$Br + O_3 \rightarrow BrO + O_2 \quad (3)$$

$$BrO + BrO \rightarrow Br_2(or\ 2Br) + O_2 \quad (4)$$

This is debated by Fan and Jacob (1992) as Br and BrO are quickly converted to non-radical bromine species and thus cannot maintain high bromine levels for ozone loss. Fan and Jacob (1992) proposed a multiphase chemistry mechanism releasing Br_2 from Br^- in acid solutions via uptake of HOBr:

$$HOBr + Br^- + H^+ \rightarrow Br_2 + H_2O \quad (5)$$

This reaction acts both an autocatalytic release of active bromine and as a recycling mechanism from nonradical species (HBr, HOBr and $BrNO_3$), which helps explain the rapid onset and maintenance of high bromine levels during the ODEs.

A number of studies have found that ODEs tend to be associated with specific meteorological conditions (Tarasick and Bottenheim, 2002; Jacobi et al., 2010; Koo et al., 2012). Tarasick and Bottenheim (2002) found that the frequent ODEs at Alert, Canada are related to the local strong surface temperature inversions and cold surface temperatures. Jacobi et al. (2010) suggested that the large-scale depleted O_3 are associated with stable boundary layer conditions and low air

temperatures. Koo et al. (2012) also found significant correlation between O_3 and potential temperatures in 0-1 km in both in-situ and aircraft observation.

1.2.3 Tropospheric bromine explosions in polar spring

Bromine explosion events, often characterized as extremely high BrO concentrations, have been measured by both ground-based and spaceborne instruments over the polar regions during spring, and often coincide with ODEs (Hönninger and Platt, 2002; Wagner et al., 2001; Jones et al., 2009; Neuman et al., 2010; Salawitch et al., 2010; Theys et al., 2011; Liao et al., 2012; Peterson et al., 2017; Simpson et al., 2017; Choi et al., 2012, 2018). Hönninger and Platt (2002) showed that BrO explosion events occur mostly within the boundary layer, especially at 0-1 km, and that during a 10-day ODE the BrO levels can reach 20-30 ppt.

The commonly known sources of tropospheric bromine include bromine release from SSA, decomposition of organobromine compounds by oxidation with OH and photolysis, and downward transport from stratosphere (Sander et al., 2003). Over the polar regions, these bromine sources, however, cannot explain the extensive and frequent bromine explosion events. Several studies have proposed additional bromine sources in polar regions associated with sea ice surface, frost flowers, blowing snow SSA, or surface snow photochemistry (Oum et al., 1998; Rankin et al., 2002; Yang et al., 2008; Pratt et al, 2013). Oum et al. (1998) suggest that bromine in frozen seawater can get activated via uptake of O_3:

$$O_3 + Br^- \rightarrow OBr^- + O_2 \quad (6)$$

$$OBr^- + H^+ \rightarrow HOBr \quad (7)$$

The HOBr can further release bromine via multiphase reaction (5).

Rankin et al. (2002) showed that the measured bromide concentrations in frost flowers are ~3 times higher than the seawater, and that frost flower have large surface area for multiphase chemistry to occur, suggesting that frost flowers can be a potential source of tropospheric bromine over the Arctic.

The sea ice and frost flowers sources of tropospheric bromine have been questioned in Pratt et al. (2013), who suggests that the high pH low Br^-/Cl^- ratio in frost flower and brine on sea ice surface make them unlikely to be the direct source of reactive bromine over the polar regions. Instead, they proposed a photochemical mechanism which can lead to production of molecular bromine when exposing saline surface snow to sunlight (Pratt et al., 2013).

Yang et al. (2008) suggested that SSA can be produced via blowing snow events and that the bromide in SSA can get released via heterogeneous reactions. Consistent with this hypothesis, Liao et al. (2012) observed lower HOBr and higher BrO levels than predicted in presence of high winds, which is in favor of blowing snow events, at springtime Barrow, Alaska.

More description on bromine release from sea ice and its impact on the halogen chemistry in the Arctic boundary layer can be found in Chapter 3.

CHAPTER 2

USING CALIOP TO CONSTRAIN BLOWING SNOW EMISSIONS OF SEA SALT AEROSOLS OVER THE ARCTIC AND ANTARCTIC SEA ICE

This Chapter is under review in *Atmospheric Chemistry and Physics*.

Huang, J., Jaeglé, L., and Shah, V.: Using CALIOP to constrain blowing snow emissions of sea salt aerosols over Arctic and Antarctic sea ice, Atmos. Chem. Phys., 18, 16253-16269, https://doi.org/10.5194/acp-18-16253-2018, 2018.

Abstract

Sea salt aerosols (SSA) produced on sea ice surfaces by blowing snow events or lifting of frost flower crystals have been suggested as important sources of SSA during winter over polar regions. The magnitude and relative contribution of blowing snow and frost flower SSA sources, however, remain uncertain. In this study, we use 2007–2009 aerosol extinction coefficients from the Cloud-Aerosol Lidar with Orthogonal Polarization (CALIOP) instrument onboard the Cloud-Aerosol Lidar and Infrared Pathfinder Satellite Observation (CALIPSO) satellite and the GEOS-Chem global chemical transport model to constrain sources of SSA over Arctic and Antarctic sea ice. CALIOP retrievals show elevated levels of aerosol extinctions (10–20 Mm^{-1}) in the lower troposphere (0–2 km) over polar regions during cold months. The standard GEOS-Chem model underestimates the CALIOP aerosol extinctions by 50–70%. Adding frost flower emissions of SSA fails to explain the CALIOP observations. With blowing snow SSA emissions, the model captures the overall spatial and seasonal variation of CALIOP aerosol extinctions over the polar

regions, but underestimates aerosol extinctions over Arctic sea ice in fall–early winter and overestimates winter-spring extinctions over Antarctic sea ice. We infer the monthly surface snow salinity on first-year sea ice required to minimize the discrepancy between CALIOP extinctions and the GEOS-Chem simulation. The empirically-derived snow salinity shows a decreasing trend between fall and spring. The optimized blowing snow model with inferred snow salinities generally agrees with CALIOP extinction observations to within 10% over sea ice, but underestimates aerosol extinctions over the regions where frost flowers are expected to have a large influence. Frost flowers could thus contribute indirectly to SSA production by increasing the local surface snow salinity and, therefore, the SSA production from blowing snow. We carry out a case study of an Arctic blowing snow SSA feature predicted by GEOS-Chem and sampled by CALIOP. Using backtrajectories, we link this feature to a blowing snow event which occurred 2 days earlier over first-year sea ice and was also detected by CALIOP.

2.1 Introduction

Sea salt aerosols (SSA) are produced via wave breaking in the open ocean (Lewis and Schwartz, 2004; De Leeuw et al., 2011 and references therein). Over polar regions, SSA can also be generated via sublimation of saline blowing snow (Simpson et al., 2007; Yang et al., 2008), wind-blown frost flower crystals (Rankin et al. 2000; Domine et al., 2004; Xu et al. 2013), and by leads in sea ice (Nilsson et al., 2001; May et al, 2016). SSA production from blowing snow events requires strong winds (> 7 m/s) and depends on the salinity of snow cover on sea ice (Yang et al., 2008). Frost flowers grow over new sea ice formed from open leads under low ambient temperature (< –20^{o}C) (Kaleschke et al., 2004). These two sea ice sources of SSA have been proposed to help explain polar observations of wintertime maxima in SSA mass concentrations (Wagenbach et al., 1998; Weller et al., 2008; Jourdain et al., 2008; Udisti et al., 2012; Huang and Jaeglé, 2017), the depletion of sulfate-to-sodium mass ratio in winter SSA relative to bulk sea water at sites in Antarctica (Wagenbach et al., 1998; Rankin et al., 2000; Jourdain et al., 2008; Hara et al., 2012) and some sites in the Arctic (Jacobi et al., 2012; Seguin et al., 2014), as well as the increase in Na^{+} deposition fluxes during glacial periods relative to interglacial periods (Wolff et al. 2006; Fischer et al., 2007; Abram et al., 2013).

In a previous study (Huang and Jaeglé, 2017), we used the GEOS-Chem chemical transport model to examine the relative roles of blowing snow and frost flowers as sources of polar SSA during winter. Our study was based on the blowing snow parameterization developed by Yang et al. (2008) and the frost flower parameterization of Xu et al. (2013). We compared our simulations to in situ observations of SSA mass concentrations at three surface sites in the Arctic and two sites in coastal Antarctica, showing that blowing snow appeared to be the dominant source of polar SSA during winter. Here, we further constrain the spatial and temporal

distribution of polar sources of SSA by using observations of aerosol extinction coefficients from the Cloud-Aerosol Lidar with Orthogonal Polarization (CALIOP) instrument onboard the Cloud-Aerosol Lidar and Infrared Pathfinder Satellite Observations (CALIPSO) satellite together with the GEOS-Chem model.

One of the main uncertainties in estimating blowing snow emissions is the salinity of snow on sea ice. In our previous work (Huang and Jaeglé, 2017), we assumed constant surface snow salinity over Arctic (0.1 practical salinity unit, or psu) and Antarctic (0.03 psu) sea ice. In reality, surface snow salinity is highly variable in time and space. The sources of sea salt in snow over sea ice include upward migration of brine from the sea ice surface, incorporation of frost flowers and SSA deposition from the nearby open ocean (Domine et al., 2004). Initial sea ice formation is accompanied by upward salt transport, such that first-year sea ice (FYI) has a high salinity reaching 20–100 psu at the sea ice surface (Weeks and Lee, 1958; Martin, 1979; Weeks and Ackley, 1986). Nakawo and Sinha (1981) found that sea ice salinity decreases rapidly within the first week of sea ice formation in fall, and then decreases more slowly between December and May in the Canadian Arctic. Worby et al. (1998) showed that ice with a thickness of less than 0.05 m displayed salinities of 9–28 psu, while ice thicker than 0.05 m had salinities of 4–8 psu, which decreased linearly with ice thickness. As snow accumulates on FYI throughout winter, the brine is wicked upward resulting in brine-wetted snow (Barber et al., 1995). Snow salinity is highest in the first 10 cm above FYI, with values of 1–20 psu (Geldsetzer et al., 2009) and then decreases rapidly as the snow cover gets thicker, with low salinities on the surface of thick snow (Nandan et al., 2017). Older and thicker multiyear sea ice (MYI), is desalinated by flushing and gravity drainage during repeated summer melt cycles, such that the overlaying snow has very low salinity. Krnavek et al. (2012) reported that surface snow salinity sampled on MYI was 0.01

psu, compared to 0.1 psu for snow on thick FYI and 0.8 psu on recently frozen thin FYI in March near Barrow, Alaska.

The role of frost flowers as a direct source of SSA remains subject to debate. Some studies have shown that strong winds inhibit frost flower formation and bury existing frost flowers with snow (Perovich and Richeter-Menge, 1994; Rankin et al., 2000), while field experiments show that frost flowers are difficult to break (Domine et al., 2005; Alvarez-Avilez et al., 2008; Obbard et al. 2009). In addition, laboratory experiments show that evaporating frost flowers form a cohesive chunk of salt (Yang et al., 2017), which is unlikely to be a direct source of SSA even when exposed to large wind speeds (Roscoe et al., 2011).

In this work, we use 3 years (2007–2009) of CALIOP aerosol extinctions to constrain the spatial and temporal distribution of polar SSA emissions with the GEOS-Chem model. Satellite observations and GEOS-Chem simulations are described in section 2. In Chapter 2.3, we evaluate the model's ability to reproduce observed aerosol extinctions over the Arctic and Antarctic sea ice regions with and without sea ice sources of SSA. In Chapter 2.4, we develop an empirical parameterization of seasonally-varying surface snow salinity on FYI. In Chapter 2.5, we conduct a case study of an Arctic blowing snow event and the resulting SSA observed by CALIOP.

2.2 Observation and model simulations

2.2.1 CALIOP observations

The CALIOP Lidar measures backscatter signals of optical pulses at 532 and 1064 nm (Winker et al., 2009). CALIOP samples the optical properties of clouds and aerosols during daytime and nighttime with a 16-day repeat cycle. It has a sampling resolution of 335 m horizontally and 30 m vertically below 30–40 km altitude. In this study, we use vertical profiles of 532 nm aerosol extinctions from CALIOP Level 2 (L2) version 4.10 profile data for 2007–2009 (Winker, 2016). L2 data is retrieved with a set of algorithms, which identify the cloud and aerosol layers and classify their feature types (Liu et al., 2009). The layer detection algorithm is performed downward for single shots and profiles are averaged horizontally at 1, 5, 20 and 80 km to achieve good signal-to-noise-ratio (SNR) for aerosol retrievals (Winker et al., 2009). The estimated detection sensitivity of the CALIOP 532-nm channel varies with different horizontal averaging, with better sensitivity at larger horizontal averaging (80 km). Nighttime CALIOP extinction coefficients have better sensitivity than daytime observations, which are affected by noise from solar radiation scattering (Winker et al., 2009).

We average monthly CALIOP L2 aerosol extinction profiles poleward of 60º over a 2° latitude by 5° longitude horizontal grid in 60 m vertical bins, using the same approach as Winker et al. (2013). When no aerosols are detected and the layer is classified as "clear air", we assign it an extinction coefficient value of 0.0 km^{-1}. Following Winker et al. (2013), we exclude the following aerosol layers from our gridded averages: (1) all aerosol layers within 60 m of the surface to avoid surface contamination, (2) layers with a Cloud Aerosol Discrimination (CAD) score falling outside the range of −100 to −20, (3) aerosol layers with uncertainty flags of 99.9 km^{-1} and the layers beneath, (4) extinction QC flags indicating possible large errors, (5) "clear air" under the lowest detected aerosol layer with base below 250 m to avoid low bias for undetected surface-attached aerosol. In addition, we exclude very high values of aerosol

extinctions (> 0.35 km^{-1}) below 2 km poleward of 60° during cold months (September–May for the Arctic and March–November for the Antarctic), as they are likely related to diamond dust misclassified as aerosol (Di Pierro et al., 2013).

The CALIOP nighttime retrievals over polar regions are limited during summer months (May–July in the Arctic, November–January in the Antarctic), with maximum latitudinal extents of 55° latitude beyond which only daytime retrievals are available. Daytime retrievals have higher detection thresholds and can only detect aerosol layers with relatively high extinctions. Therefore, at a given latitude fewer aerosol layers are detected in the daytime retrievals, and the average daytime extinction coefficients are lower than the nighttime ones over polar regions. Most of our work is based on analysis of nighttime CALIOP retrievals during winter over polar regions. However, to reconstruct the full seasonal cycle of aerosol extinctions over polar regions, we calculate nighttime equivalent aerosol extinction profiles by combining both daytime and nighttime CALIOP extinctions coefficients, following the algorithm described in Di Pierro et al. (2013). This approach provides an empirical correction for the differences in detection sensitivity and aerosol extinctions in the daytime CALIOP retrievals.

2.2.2 The GEOS-Chem chemical transport model

We use the GEOS-Chem (v10-01) 3-D global chemical transport model (Bey et al., 2001) driven by meteorological fields from the Modern Era Retrospective-Analysis for Research and Applications (MERRA; Rienecker et al., 2011). The MERRA assimilated meteorological fields have a native horizontal resolution of 0.5° latitude by 0.666° longitude with 72 vertical levels,

which we regrid to 2°×2.5° horizontal resolution and 47 vertical levels with merged levels above 80 hPa.

We conduct a three-year (2007–2009) global simulation of tropospheric aerosol-oxidant chemistry. The model is initialized with a 1-year spin up. Global anthropogenic emissions are from EDGAR v4.2 (Emissions Database for Global Atmospheric Research, Olivier and Berdowski, 2001) for 1970–2008. For the years after 2008, anthropogenic emissions are scaled relative to year 2008, based on government statistics for different countries/regions (van Donkelaar et al., 2008). Over North America, the anthropogenic emissions are from the 2011 National Emissions Inventory (NEI2011; https://www.epa.gov/air-emissions-inventories/2011-national-emissions-inventory-nei-data) produced by the US Environmental Protection Agency (EPA), with annual scaling factors from the EPA for other years. Over Asia, the anthropogenic emissions are from the MIX emission inventory (Li et al., 2017). Over Europe, we use the Co-operative programme for monitoring and evaluation of long range transmission of air pollutants in Europe (EMEP) anthropogenic emissions (http://www.ceip.at/review-of-inventories/). Monthly biomass burning emissions are from the Global Fire Emissions Database version 4 (GFEDv4, van der Werf et al., 2010). Black carbon (BC) and organic carbon (OC) emissions are based on the Bond et al. (2007) monthly emission inventory, including sources from fossil fuel and biofuel. Dust emissions are based on the dust entrainment and deposition scheme from Zender et al. (2003). Biogenic emissions of volatile organic compounds (VOCs) are from the Model of Emissions of Gases and Aerosols from Nature version 2.1 (MEGAN 2.1, Guenther et al., 2012). The HO_x-NO_x-VOC-O_3-BrO_x tropospheric chemistry chemical mechanism is described in Mao et al. (2010, 2013) with recent updates in biogenic VOC chemistry (Fisher et al., 2016; Travis et al., 2016). The gas-particle partitioning of SO_4^{2-}-NO_3^--NH_4^+ aerosol is

computed with the ISORROPIA II thermodynamic module (Fountoukis and Nenes, 2007), as implemented by Pye et al. (2009).

The open-ocean emissions of SSA are a function of wind speed and sea surface temperature (SST) as described in Jaeglé et al. (2011). In Huang and Jaeglé (2017), we inferred that wave-breaking SSA emissions are suppressed during summer at coastal polar sites with cold waters (SST < 5°C). As in Huang and Jaeglé (2017), we reduce SSA emissions for these cold waters. We use two SSA size bins: accumulation mode (r_{dry} = 0.01−0.5 μm) and coarse mode (r_{dry} = 0.5–8 μm).

Advection is based on the Lin and Rood (1996) advection algorithm and boundary layer mixing is computed using the non-local scheme in Lin and McElroy (2011). Dry deposition in the GEOS-Chem follows a standard resistance-in-series scheme based on Wesely (1989) as described by Wang et al. (1998). Dry deposition of SSA in the model follows the Zhang et al. (2001) size-dependent scheme over land, and is calculated based on the Slinn and Slinn (1980) deposition model over ocean and sea ice, as implemented by Jaeglé et al. (2011) in GEOS-Chem. The strong size-dependence of SSA deposition is taken into account by integrating the dry deposition velocity over each of the 2 SSA size bins using a bimodal size distribution including growth as a function of local relative humidity (RH). Sedimentation of SSA is calculated throughout the atmospheric column based on the Stokes velocity scheme. Wet deposition of aerosol includes convective updraft, washout and rainout from precipitation (Liu et al., 2001), as well as snow scavenging (Wang et al., 2011).

The blowing snow SSA emissions in GEOS-Chem is based on the parameterizations of Yang et al. (2008, 2010) as implemented by Huang and Jaeglé (2017). The SSA production from

blowing snow is a function of RH, temperature, age of snow, snow salinity, and wind speed. The size distribution of wind-lifted snow particles follows a two-parameter gamma distribution (Yang et al., 2008 and references therein). Once sublimated, snow particles are released as SSA particles. We assume that 5 SSA particles are produced per snowflake (N=5) based on a comparison against observations of submicron SSA mass concentrations at Barrow, Alaska (Huang and Jaeglé, 2017). The size distribution of blowing snow SSA is determined from the size distribution of snow particles, N (=5), and salinity. The resulting emitted mass of blowing snow SSA is obtained by integrating this size distribution into the two SSA size bins. In our previous work, we had assumed a uniform salinity on Arctic (0.1 psu) and Antarctic sea ice (0.03 psu) based on mean observations of surface snow salinity (Mundy et al., 2005; Krnavek et al., 2012). Here we use these salinities for FYI, but now take into account the lower surface snow salinity of older sea ice, by assuming that MYI snow salinity is 10 times lower than on FYI (Krnavek et al., 2012): 0.01 psu on Arctic MYI snow and 0.003 psu on Antarctic MYI snow. We calculate a mean snow age of 3 days for the Arctic and 1.5 days for the Antarctic from MERRA.

Frost flower SSA emissions follows the emission scheme of Xu et al. (2013), which follows the empirical wind-dependence of Shaw et al. (2010) and the potential frost flower (PFF) coverage of Kaleschke et al. (2004). The PFF is a function of ambient air temperature, and frost flowers are formed on very new and young sea ice once the ambient air temperature is cold enough (< about –20°C). We set a threshold of 10 cm for the thickness of newly formed sea ice beyond which we assume that frost flowers do not form due to inefficient brine transport through thicker sea ice. The size distribution of SSA from frost flowers follows a lognormal size distribution with a geometric mean diameter of 0.015 μm and a geometric standard deviation of 1.9 (Xu et

al., 2013). This size distribution is integrated into the two GEOS-Chem SSA size bins to obtain the emitted mass of SSA from frost flowers.

The sea ice concentration boundary conditions in MERRA are derived from the weekly product of Reynolds et al. (2002), which is based on Special Sensor Microwave Imager (SSMI) instruments on Defense Meteorological Satellite Program (DMSP) satellites. The weekly products have an original spatial resolution of 1°×1°, and are linearly interpolated in time to each model time step. For each year, we use the preceding summertime minimum sea ice extent in MERRA (September in the Arctic and February in the Antarctic) to infer the location of MYI. FYI extent is calculated by subtracting MYI extent from total sea ice extent.

In this study, we neglect the role of leads as a source of SSA as we found in Huang and Jaeglé (2017) that while this additional source could potentially be important on local scales near leads, overall the regional increase in SSA emissions is less than 10%.

Our standard simulation (STD) includes tropospheric aerosol-oxidant chemistry and SSA emissions from the open ocean. The STD+Snow simulation is the STD simulation to which we add SSA emissions from blowing snow as in Huang and Jaeglé (2017), with surface snow salinities as described above (0.1 psu on FYI and 0.01 psu on MYI over the Arctic, and 0.03 psu on FYI and 0.03 psu on MYI over the Antarctic). The STD+FF simulation is the STD simulation with SSA emissions from frost flowers. In Section 4, we develop an optimized blowing snow simulation (STD+Opt. Snow), with seasonally varying snow salinity on FYI.

The GEOS-Chem simulations are sampled at the time and location of the CALIOP overpasses and averaged over the same horizontal and vertical grid. For comparison to CALIOP

observations, we apply the CALIOP nighttime detection threshold to the model, setting the modeled backscatter coefficients to 0 Mm^{-1} sr^{-1} for backscatter values lower than 0.2 Mm^{-1} sr^{-1}.

2.3 Model evaluation with CALIOP observations

2.3.1 Arctic

The Arctic cold season (November–April) CALIOP extinction coefficients in the lower troposphere (0–2 km above sea level, asl) display values of 10–30 Mm^{-1} (Figure 2.1a). The largest extinction coefficients occur over the open-ocean regions of the Greenland and Barents Seas. In addition, significant aerosol extinction coefficients (10–20 Mm^{-1}) are seen over the sea ice covered Chukchi Sea, East Siberian Ocean, Laptev Sea, Kara Sea and Canadian Arctic Archipelago (Figure 2.1a). While the STD GEOS-Chem simulation reproduces the pattern of extinctions over the open ocean regions, it fails to capture the enhancements over sea ice, underestimating aerosol extinction coefficients by ~10 Mm^{-1} over the central Arctic (Figure 2.1b). The normalized mean bias (NMB=$100\times(\overline{Model}/\overline{Obs}-1)$, with $\overline{Model}$ and $\overline{Obs}$ representing mean observed and modeled values) is –55% over FYI, and –68% over MYI (Figure 2.2a). GEOS-Chem also underestimates CALIOP aerosol extinctions over Northern Russia, which could be due to missing sources of aerosols and their precursors from gas flaring in the region (Li et al., 2016; Klimont et al., 2017; Xu et al., 2017).

In the STD simulation, aerosol extinction coefficients during the cold season are dominated by SSA over the high latitude open ocean and by long-range transport of sulfate aerosols over sea ice (Figure 2.1f and g). Adding blowing snow emissions of SSA increases the simulated aerosol

extinctions by ~10 Mm^{-1} over the central Arctic, bringing the STD+Snow simulation in better agreement with CALIOP observations (Figure 2.1c and h), with a model bias of –7% on FYI and –17% on MYI (Figure 2.2b). Inclusion of frost flower emissions of SSA in the STD+FF simulation has the largest influence over Canadian Arctic Archipelago where cold temperatures and open leads co-exist (Figure 2.1j), but the overall magnitude of the increase cannot explain the CALIOP extinctions.

Figure 2.3 compares the vertical and seasonal distribution of aerosol extinction coefficients in the lower troposphere (0–2 km altitude) over FYI, MYI, and the Canadian Arctic Archipelago, where frost flowers are expected to have their largest influence (Huang and Jaeglé, 2017). Over all three regions, the STD simulation underestimates cold season CALIOP extinctions by factors of 3–6 (Figure 2.3d and f). The STD+FF simulation reduces the negative model bias, but the modeled extinctions remain too low by 20–40% (Figure 2.3d–f). Furthermore, the STD+FF simulation does not capture the rapid increase in CALIOP extinctions in October–December (Figure 2.3g–i). We find that applying a single scaling factor to the frost flower emissions cannot address the seasonally-varying model discrepancy. In comparison, the STD+Snow simulation displays the best agreement with the CALIOP observations, reproducing both the vertical profile and seasonal cycle of CALIOP extinctions. The STD+Snow simulation, however, underestimates the CALIOP aerosol extinctions in October–December by 30–50% (Figure 2.3g and f), and underestimates the surface CALIOP cold season aerosol extinctions by up to 5 Mm^{-1} (Figure 2.3d and e). In addition, it predicts a maximum in aerosol extinction during April, while CALIOP observations display their largest concentrations in January–March for FYI, and in March over MYI.

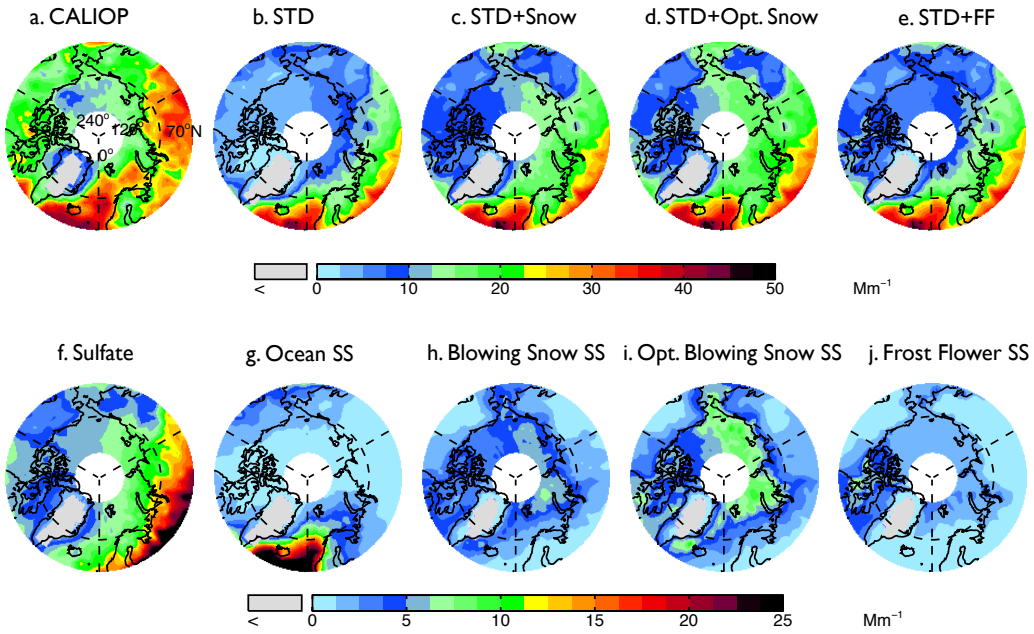

Figure 2.1: Spatial distribution of mean aerosol extinction coefficients (0-2 km) during the 2007-2009 Arctic cold season (November-April) observed by (a) CALIOP and calculated with the GEOS-Chem model in (b) a Standard simulation (STD), (c) a simulation including blowing snow SSA emissions (STD+Snow), (d) an optimized blowing snow simulation (STD+Opt. Snow), and (e) a simulation including frost flower SSA emissions (STD+FF). The simulated extinctions are sampled at the time and location of the CALIOP overpasses, and the CALIOP sensitivity threshold is applied. The bottom panels show the extinction coefficients of individual aerosol components in the GEOS-Chem simulations: (f) sulfate aerosol, (g) open ocean SSA, (h) blowing snow SSA, (i) Opt. blowing snow SSA and (j) frost flower SSA. Note the different colorbar scales for the top and bottom rows.

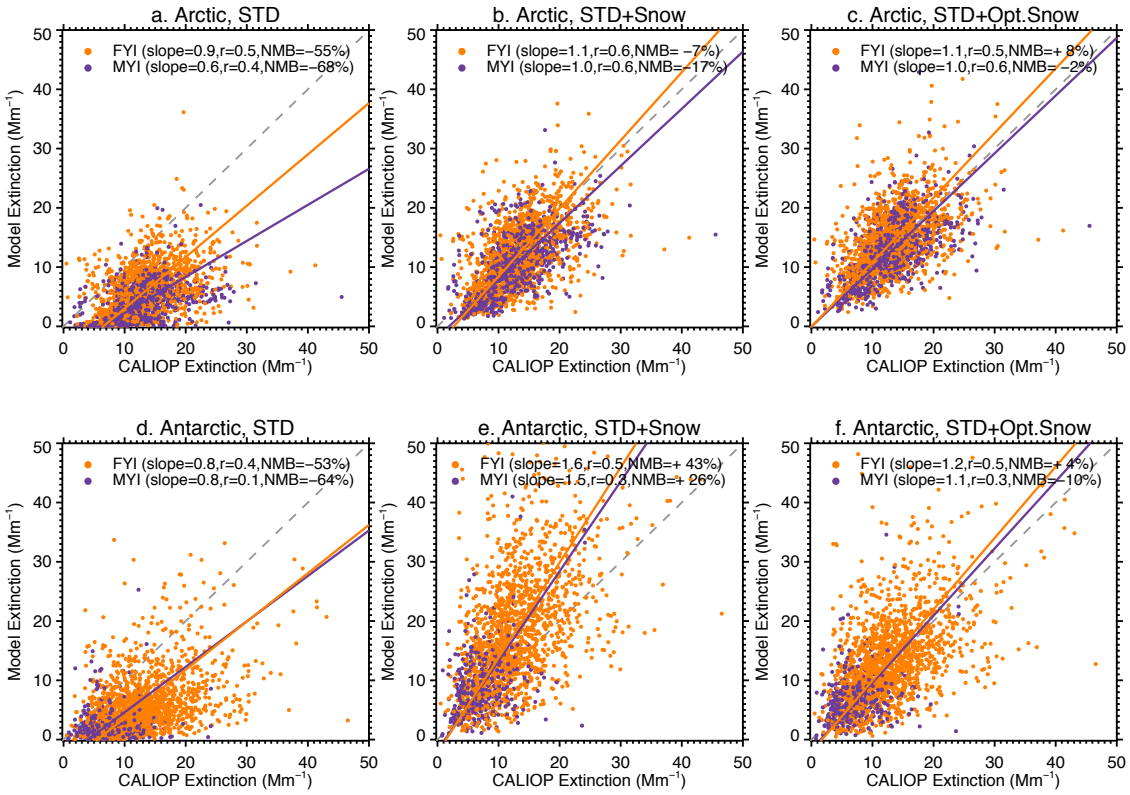

Figure 2.2. Scatter plot of CALIOP and GEOS-Chem aerosol extinction coefficients over FYI (orange circles) and MYI (purple circles) for the Arctic cold season (November–April, top panels) and Antarctic cold season (May–October, bottom panels). Each symbol represents the monthly aerosol extinction coefficients for individual grid boxes (2°x5°, 0–2 km) over sea ice. The dashed gray line is the 1:1 line. The purple and orange lines are the linear fit for the points over MYI and FYI, respectively. The slope of the regression line, correlation coefficient (r) and normalized mean bias, $\mathbf{NMB} = \mathbf{100}\times(\overline{\mathbf{Model}}/\overline{\mathbf{Obs}} - \mathbf{1})$, are given in the insert of each figure.

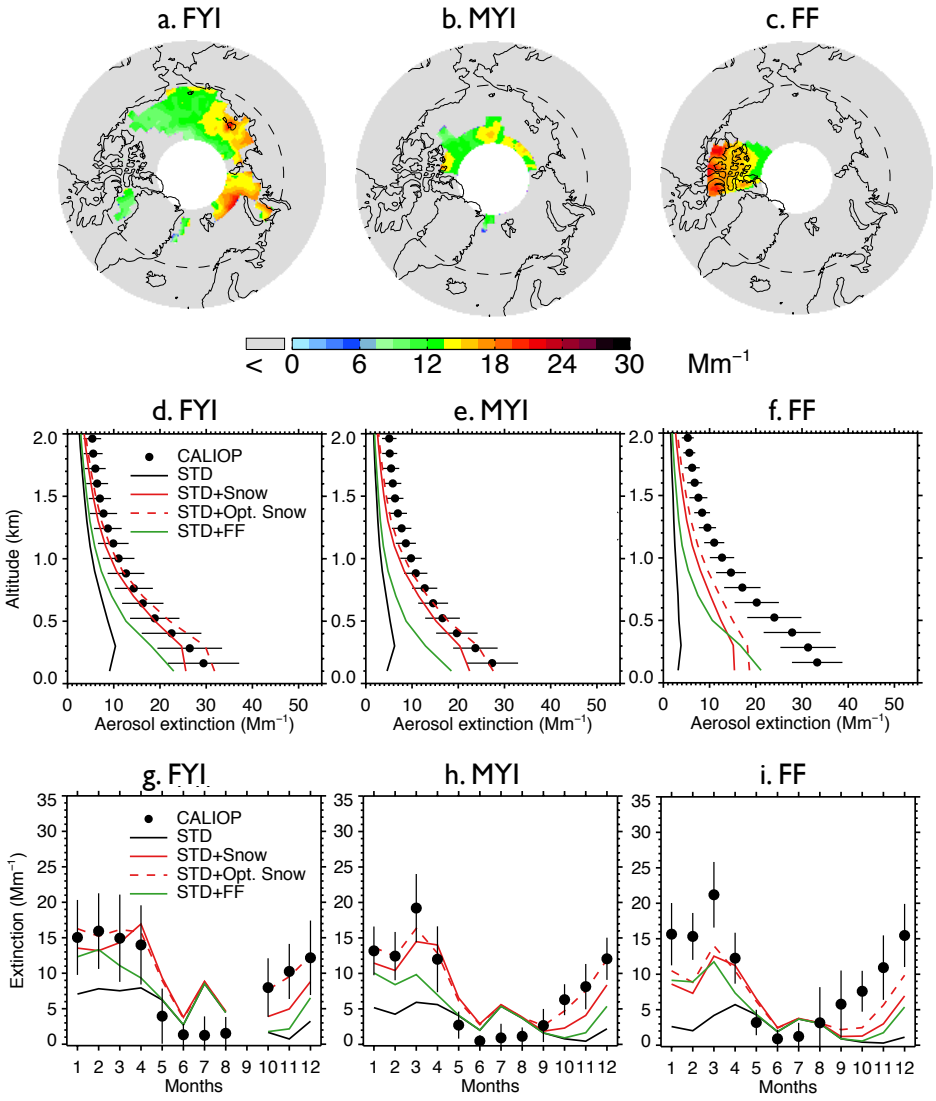

Figure 2.3: Top row: 2007–2009 CALIOP mean aerosol extinction coefficients (0–2 km) in the Arctic cold season (November–April) over (a) first-year sea ice (FYI), (b) multi-year sea ice (MYI) and (c) the Canadian Arctic Archipelago (CAA). Middle row: Vertical profiles of Arctic cold season mean aerosol extinction coefficients over (d) FYI, (e) MYI and (f) CAA for CALIOP (black dots with horizontal lines indicating standard deviations) and GEOS-Chem model simulations (STD: black lines, STD+Snow: red solid lines, STD+Opt. Snow: red dashed lines; STD+FF: green lines). Bottom row: Seasonal cycle of 0–2 km monthly aerosol extinction coefficients averaged

over (g) FYI, (h) MYI and (f) CAA. CALIOP observations are shown as black circles and vertical lines indicate the interannual standard deviation. The four GEOS-Chem model simulations are also shown (STD: black lines, STD+Snow: red solid lines, STD+Opt. Snow: red dashed lines, STD+FF: green lines).

2.3.2 Antarctic

During the Austral cold season (May–October), CALIOP aerosol extinction coefficients decrease with increasing latitudes, ranging from 20–30 Mm^{-1} at 60ºS to 5–10 Mm^{-1} near coastal Antarctica (Figure 2.4a). Over Antarctic FYI (Figure2.5a), CALIOP aerosol extinctions display values of 10–14 Mm^{-1} in July–October in the lower troposphere (Figure 2.5g), with aerosol extinctions attaining 30 Mm^{-1} near the surface (Figure 2.5d). Over MYI sea ice offshore of the Ronne ice-shelf, the CALIOP extinctions are somewhat smaller, reaching 20 Mm^{-1} near the surface (Figure 2.5e).

Poleward of 70°S, open ocean SSA dominate aerosol extinction coefficients in the STD simulation (Figure 2.4f), accounting for 80% of the extinction, with the remaining 20% due to the combined contributions from sulfate, black carbon and organic aerosols. The STD simulation underestimates CALIOP observations by 5–10 Mm^{-1} (Figure 2.5g–i), with a –53% bias over FYI and a –64% bias over MYI (Figure 2.2d). The inclusion of frost flowers in the STD+FF simulation leads to a ~2 Mm^{-1} increase in extinction coefficients near the Ross and Ronne Ice-shelves where cold temperatures and open leads persist (Figure 2.4i). This increase is insufficient to explain CALIOP observations (Figure 2.4e and 2.5).

The STD+Snow simulation increases aerosol extinction coefficients by 10-20 Mm^{-1} in the Indian Ocean (0–100°) and Pacific Ocean (180–270°) sectors (Figure 2.4g), where strong winds persist. We find that the inclusion of blowing snow SSA emissions results in a 43% overestimate of CALIOP extinctions over FYI sea ice (Figure 2.2e) and too strong a seasonal increase in extinctions between May and October (Figure 2.5g). Over the smaller MYI region, the positive bias of the STD+Snow simulation is +26% (Figure 2.2e, 2.5e and h).

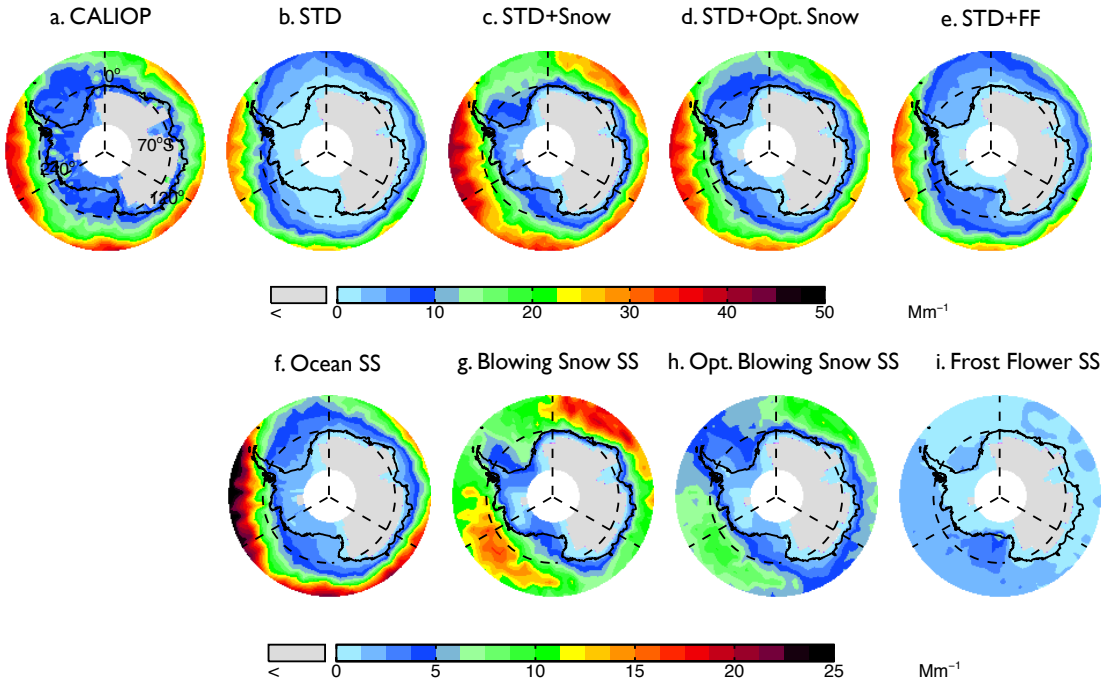

Figure 2.4. Spatial distributions of mean aerosol extinction coefficients (0–2 km) during the 2007-2009 Antarctic cold season (May–October) observed by (a) CALIOP and calculated with the GEOS-Chem (b. STD, c. STD+Snow, d. STD+Opt. Snow, e. STD+FF). The bottom panels show extinctions of individual aerosol components in the GEOS-Chem simulations: (f) open ocean SSA,

(g) blowing snow SSA, (h) Opt. blowing snow SSA and (i) frost flower SSA. Note the different colorbar scales for the top and bottom rows.

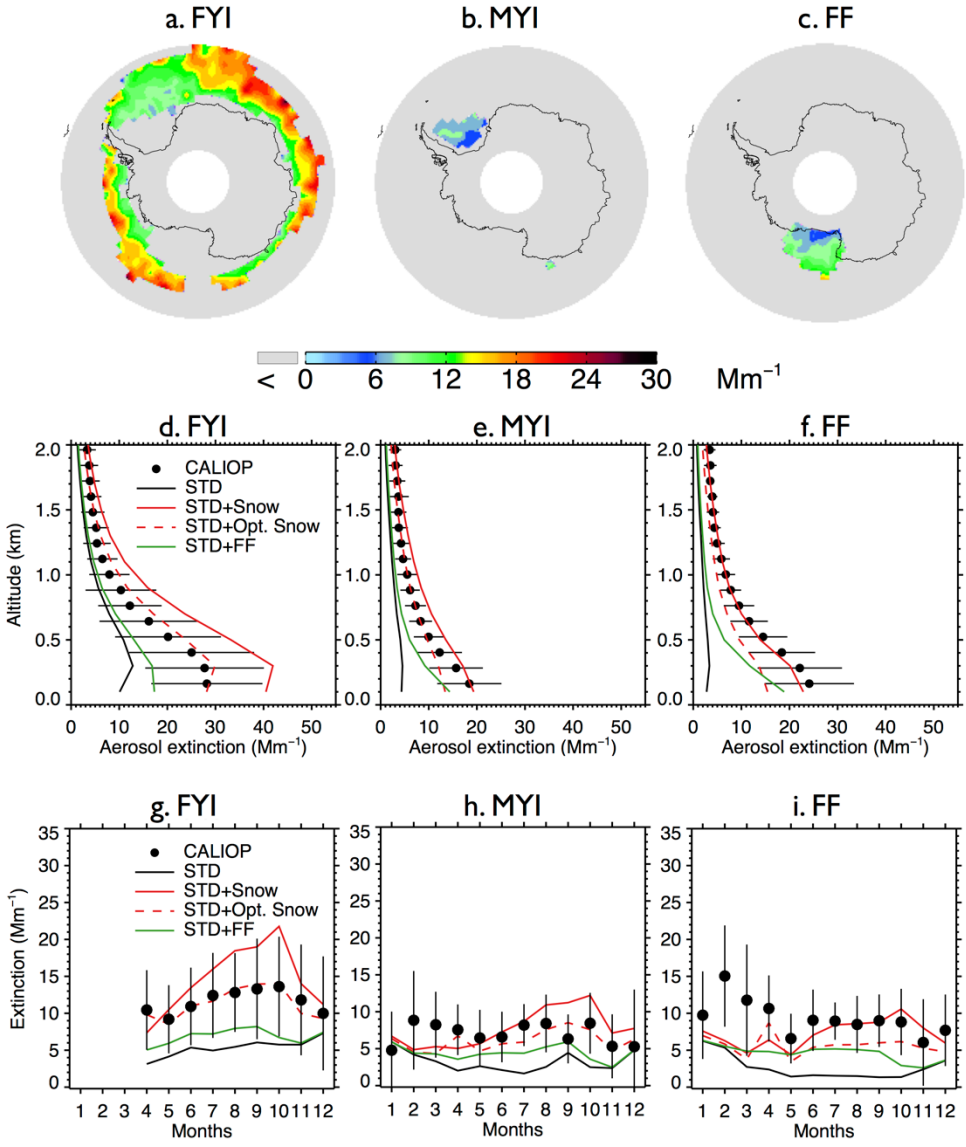

Figure 2.5. Same as Figure 2.3, but for Antarctic aerosol extinction coefficients during Austral winter (May–October) over (a) FYI (excluding offshore Ross Ice-shelf), (b) MYI and (c) offshore

Ross Ice-shelf. As shown in (g), the monthly average aerosol extinction coefficients are not available over FYI during Antarctic summer (January–March) due to the limited FYI extent.

2.4 Blowing snow simulation with optimized snow salinity

While the inclusion of blowing snow leads to improved agreement with CALIOP, we hypothesize that the remaining discrepancies in the magnitude and seasonal cycle of aerosol extinction coefficients are due to our simplifying assumption of a uniform surface snow salinity over FYI.

As discussed in Section 2.1, the surface snow salinity is highest over thin FYI with little snow cover early in the cold season, declining in the ensuing months as a result of thickening sea ice and increasing snowpack cover (Barber et al., 1995; Krnavek et al., 2012; Weeks and Lee, 1958; Weeks and Ackley, 1986; Nakawo and Sinha, 1981). As no systematic observations of surface snow salinity are available over sea ice, our approach is to find the monthly salinity of snow on FYI required to minimize the discrepancy between CALIOP extinctions and the GEOS-Chem simulation. The salinity of surface snow on MYI is the same as in the STD+Snow simulation.

By using a linear regression between the GEOS-Chem simulation and CALIOP monthly extinctions over Arctic sea ice, we derive a surface snow salinity on FYI of 0.9 psu in September, decreasing to 0.09 psu in April (with values of 0.36, 0.26, 0.19, 0.16, 0.16, and 0.14, between October and March). The inferred snow salinities decrease with time and are generally consistent with observations near Alaska reported by Krnavek et al. (2012): 0.8 psu for snow over recently frozen thin FYI and 0.1 psu over thick FYI. For Antarctic FYI, we infer snow

salinities of 0.05 psu in April, 0.02 in May–June and 0.018 in July–September. For the rest of the year the salinity is 0.015 psu. These decreasing trends in salinity between fall and spring are consistent with expectations based on the seasonal evolution of FYI thickness, sea ice surface salinity and deepening snow cover (Worby et al., 1998; Warren et al., 1999; Massom et al., 2001; Kwok and Cunningham, 2015).

We use our empirically-derived monthly snow salinities to conduct an optimized blowing snow simulation (STD+Opt. Snow). Over Arctic FYI, the model bias changes from –7% (STD+Snow) to +8% (STD+Opt. Snow), and for MYI the model bias of –17% changes to –2% (Figure 2.2b and c). Over Antarctic FYI, the model overestimate decreases from +43% (STD+Snow) to +4% (STD+Opt. Snow). Similarly, the model bias over MYI decreases to –10% (Figure 2.2e and f). The STD+Opt. Snow simulation displays cold season extinction profiles that are within 5–10% of CALIOP observations over sea ice (Figure 2.3d–e and 2.5d–e). The seasonal cycles are in better agreement with observations, especially in the Arctic for October–December when the inferred FYI salinities (0.36-0.19 psu compared to 0.1 psu in the STD+Snow simulation) lead to a near doubling of aerosol extinction (Figure 2.3g–h). Over Antarctica, the amplitude of the seasonal cycle of aerosol extinction over FYI is reduced, in better agreement with CALIOP observations (Figure 2.5g–h).

We also examined whether a single fixed value of salinity over FYI can lead to similar improvements in the agreement with CALIOP. The resulting fixed salinities are 0.11 psu over Arctic FYI and 0.018 psu over Antarctic FYI, leading to good overall agreement with CALIOP over the Antarctic (NMB of +5% on FYI and –9% on MYI) with no significant improvement seen in the Arctic (NMB of –7% on FYI and –18% on MYI). We found that over the Arctic, a simulation using a single salinity of 0.11 psu yields results similar to the STD+Snow simulation

and cannot explain the high extinction values during fall/early winter. Over Antarctic sea ice, the performance of a simulation with 0.018 psu over FYI shows results similar to the STD+Opt. Snow simulation. Thus there is a stronger case for using a seasonally varying snow salinity over Arctic sea ice than over Antarctic sea ice. We speculate that this might be linked to relatively smaller seasonal variation in sea ice thickness and snow depth for Antarctic sea ice compared to the Arctic. In their snow climatology, Warren et al. (1999) report that the mean snow depth at an Arctic sea ice site increased from 8.7 cm in October to 28.9 cm in March. Satellite-based observations of Arctic FYI thickness show an increase from 0.95 m in October to 2.15 m in May (Kwok and Cunningham, 2015). In contrast, over Antarctic sea ice the mean sea ice thickness and snow depth remained fairly constant during fall–winter (April: 0.48 m for ice thickness and 0.11 m for snow depth; August: 0.52 m for ice thickness and 0.11 m for snow depth) as described in Worby et al. (1998).

Both STD+Snow and STD+Opt. Snow models underestimate CALIOP aerosol extinctions over the Canadian Arctic Archipelago (Figure 2.3f). Combining the STD+Opt. Snow and frost flower emissions could help improve the agreement in that region, but it would also lead to substantial overestimates over FYI and MYI for the rest of the Arctic. One possibility is that snow-covered frost flowers in the Canadian Archipelago increase the local surface snow salinity (Domine et al., 2004). The recent study of Hara et al. (2017) in northwestern Greenland proposed that snowfall buries frost flowers and the associated slush layer on new FYI. The resulting brine migrates vertically enriching the surface snow layer, which can be mobilized under strong winds. We estimate that increasing the salinity of snow over the Canadian Archipelago to a value of 3 psu would help reconcile the optimized blowing snow simulation with CALIOP observations. Direct measurements of snow salinity in this region would help confirm this estimate. Similarly, we

find that increasing the snow salinity near the Ross ice-shelf region, where frost flowers are expected to occur, would improve the agreement with CALIOP observations.

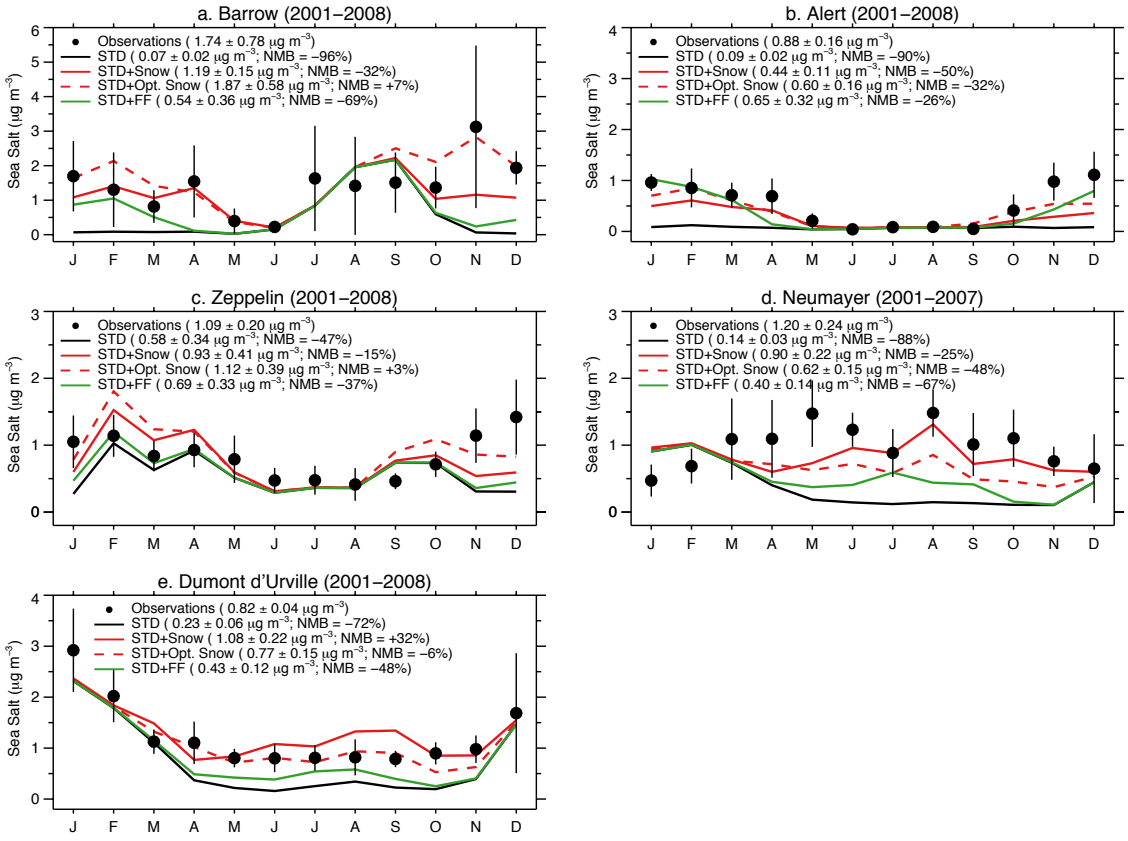

Figure 2.6. Monthly mean SSA mass concentrations at Arctic sites (a. Barrow, b. Alert, c. Zeppelin) and Antarctic sites (d. Dumont d'Urville, e. Neumayer). All observations and model results are for 2001–2008 except at Neumayer (2001–2007). The observed mean concentrations are indicated with filled black circles, and the lines are for the GEOS-Chem simulations (STD: black line, STD+Snow: red line, STD+Opt, Snow: red dashed line; STD-FF: green line). The black vertical lines are the standard deviations of monthly means for the observation years. For each

individual panel, the insert lists mean concentrations and standard deviations, as well as the NMB for the cold season only (Arctic: November–April; Antarctic: May–October).

Figure 2.6 evaluates the performance of the STD+Opt. Snow simulation against independent observations of SSA mass concentrations at Barrow, Alaska (71.3ºN, 156.6ºW); Alert, Nunavut, Canada (82.5ºN, 62.5ºW); Zeppelin, Svalbard (78.9ºN, 11.9ºE); Neumayer, Antarctica (70.7°S, 8.3°W) and Dumont d'Urville, Antarctica (66.7ºS, 140ºE). Descriptions of the in situ observations are provided in Huang and Jaeglé (2017). At Barrow, the optimized simulation improves the agreement with observed SSA mass concentrations in November–May. In particular, the enhanced salinity in October–November brings the model closer to the observations. At Zeppelin and Dumont d'Urville, the model bias in the STD+Opt. Snow simulation is reduced relative to the STD+Snow simulation. However, the model bias worsens at Neumayer (STD+Snow: –25%, STD+Opt. Snow: –48%), and the magnitude of model bias remains large at Alert (STD+Snow: –50%, STD+Opt. Snow: –32%). As Neumayer and Alert are close to the frost flower producing regions, compared to other polar sites, this underestimate may be related to an underestimate in the snow salinity in those regions.

It is also possible that the discrepancies between observed and modeled aerosol extinction coefficients are due to other factors in the blowing snow parameterization as implemented in GEOS-Chem. For example, our simulation does not include the negative feedback of water vapor sublimation (Mann et al., 2000): as blowing snow particles sublime in unsaturated air, they cause an increase in water vapor and thus cooling of the surrounding air. Both effects lead to an increase in RH near saturation, reducing the sublimation rate. Another underlying assumption is

that 5 SSA are produced for each snowflake that sublimes (N=5). We conducted a sensitivity simulation assuming one SSA per snowflake, shown as STD+Snow (N=1) in the supplement (Figure S7 and S8). This change does not affect the total emissions of blowing snow SSA, but decreases the fraction of SSA in the accumulation mode (see Huang and Jaeglé, 2017). As the extinction efficiency of accumulation mode SSA is larger than that of coarse mode SSA, the assumption of N=1 leads to a 30–50% decrease in modeled extinctions relative to the STD+Snow (N=5) simulation. Overall, this results in improved agreement with CALIOP observations over Antarctic sea ice, but the CALIOP aerosol extinctions are underestimated over the Arctic. Increasing the surface snow salinity over Arctic FYI can address the model discrepancy in aerosol extinction coefficients, but will lead to a factor of 1.5–2 overestimate in SSA mass concentrations.

2.5 A case study of a blowing snow event over the Arctic

Figure 2.7 shows a case study of a blowing snow SSA event, which occurred on November 6, 2008 over the Arctic. The STD+Snow and STD+Opt. Snow simulations show enhanced extinction coefficients (40–80 Mm^{-1}) over the Barents Sea along the 60ºE longitude line extending from the North Pole to 70ºN (Figure 2.7b and c). This feature is due to blowing snow SSA and it is not seen in the STD simulation (Figure 2.7a) or the frost flower simulation (not shown).

The CALIPSO 00:58–01:12 UTC overpass on November 6, 2008 transected this feature, with CALIOP aerosol extinction coefficients of 50–150 Mm^{-1} between points A (78°N; 52.5°E) and B (82° N; 110° E) labelled in Figure 2.7a–c. The cross section along the CALIOP overpass shows

that the large extinctions are confined between the surface and 1–2 km altitude (Figure 2.7e). This overpass region is mostly covered by FYI (Figure 2.7d). We sampled GEOS-Chem along the same cross section, finding a very good correspondence in the spatial extent of the feature observed by CALIOP and simulated by the STD+Snow and STD+Opt. Snow simulations (Figure 2.7g–i). The optimized blowing snow model predicts higher aerosol extinctions due to larger surface snow salinity on FYI in November, and is in better agreement with the 0–2 km CALIOP mean aerosol extinction coefficients (Figure 2.7i).

We use the FLEXPART particle dispersion model (Stohl et al., 1998, 2005; Seibert and Frank, 2004) with meteorological data from ERA-Interim with a horizontal resolution of 0.5° to track the origin of this feature. We release 100,000 particles between points A and B at 0.01–2km and track them back in time over 2 days. The air along the AB transect in Figure 2.7 originates from the 120–140°E sector at 60°–90°N near the surface (0–100 m), on November 4, 2008 (Figure 2.8a). This region is covered by both MYI and FYI (Figure 2.7d). The STD+Snow model predicts enhanced blowing snow emissions in this region on November 4, 2008 (Figure 2.8b). The CD transect in Figure 2.8b shows the CALIOP overpass at 01:11–01:24 UTC November 4, 2008. This CALIOP transect displays elevated 532 nm attenuated perpendicular backscatter and depolarization ratio below 200 m (Figure 2.8c and d), which are co-located with strong surface winds (>5 m s^{-1}). The pattern of elevated backscatter, surface winds and depolarization ratio satisfies the requirements of the CALIOP blowing snow detection algorithm described in Palm et al. (2011, 2017), who defined blowing snow events as layers with high color ratio (>1), high depolarization ratio (>0.25), strong surface winds (>4 m s^{-1}), and enhanced backscatter signals below 300 m (ranging between 2.5×10^{-2} km^{-1} sr^{-1} and 0.2 km^{-1} sr^{-1}). Therefore, the FLEXPART-predicted source region and CALIOP blowing snow feature are co-located with enhanced

blowing snow emissions in the GEOS-Chem simulation (Figure 2.8b). This case study thus shows that CALIOP can detect not only the blowing snow event (Palm et al., 2011) but also the resulting SSA produced after sublimation.

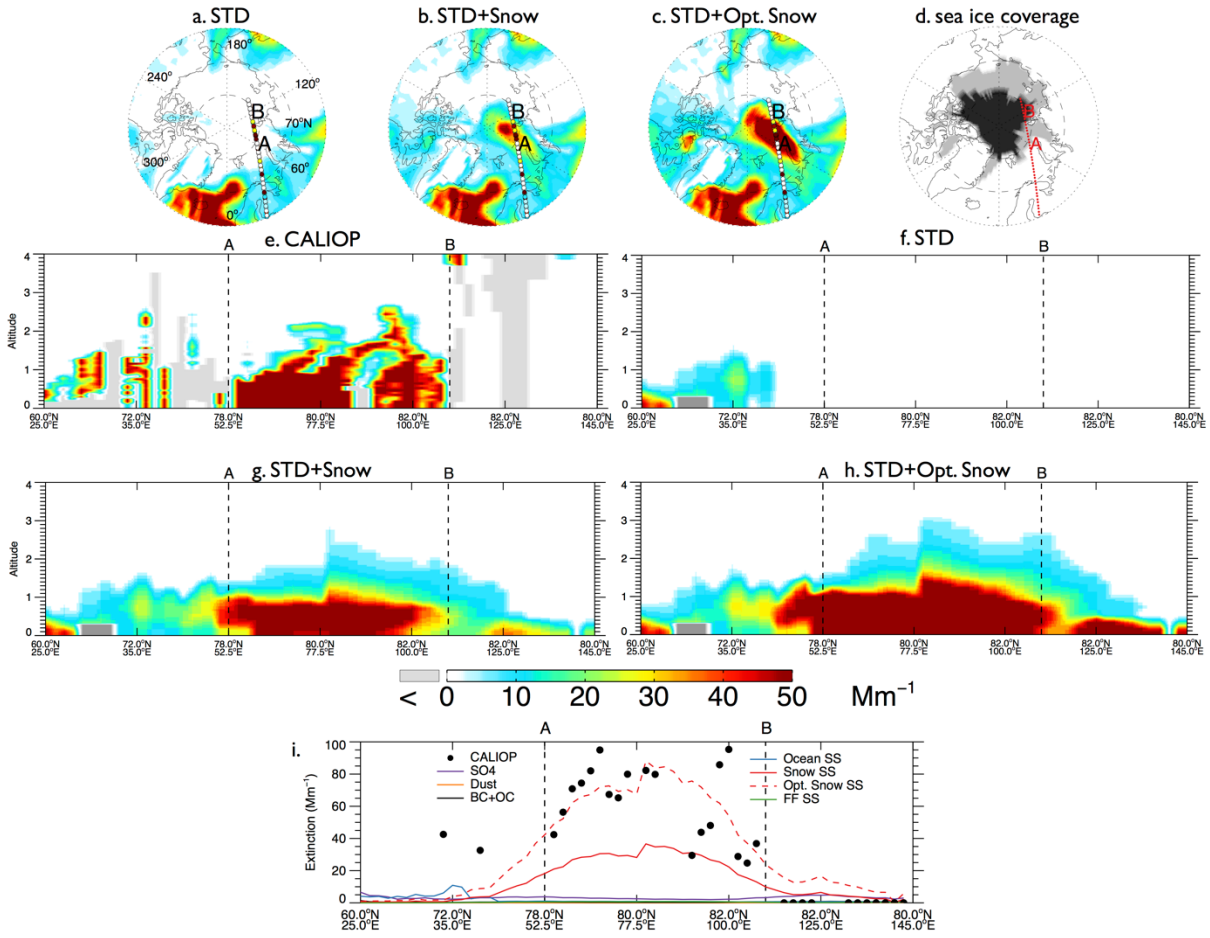

Figure 2.7. November 6, 2008 case study of a blowing snow SSA feature over the Arctic. Top panels: Spatial distribution of mean aerosol extinctions below 2 km altitude for the (a) STD, (b) STD+Snow, and (c) STD+Opt. Snow GEOS-Chem simulations. The CALIOP nighttime overpass at 00:58–01:12 UTC is displayed on the top panels, with filled circles color-coded according to observed mean extinction coefficients below 2 km. The overpass intercepts the SSA blowing snow feature between points A and B. Panel (d) shows the MERRA sea ice coverage on November 6,

2008, with light gray shading indicating FYI and black shading for MYI. Panels (e–h) show the observed and simulated vertical cross-sections of aerosol extinction coefficients along the CALIOP overpass. The light gray shading in (e) indicates that no valid data is available for CALIOP. The dark gray shading in (f–h) shows the local topography in the model. Panel (i) shows the 0–2 km CALIOP mean aerosol extinctions and the contributions of different aerosol types in the GEOS-Chem simulations.

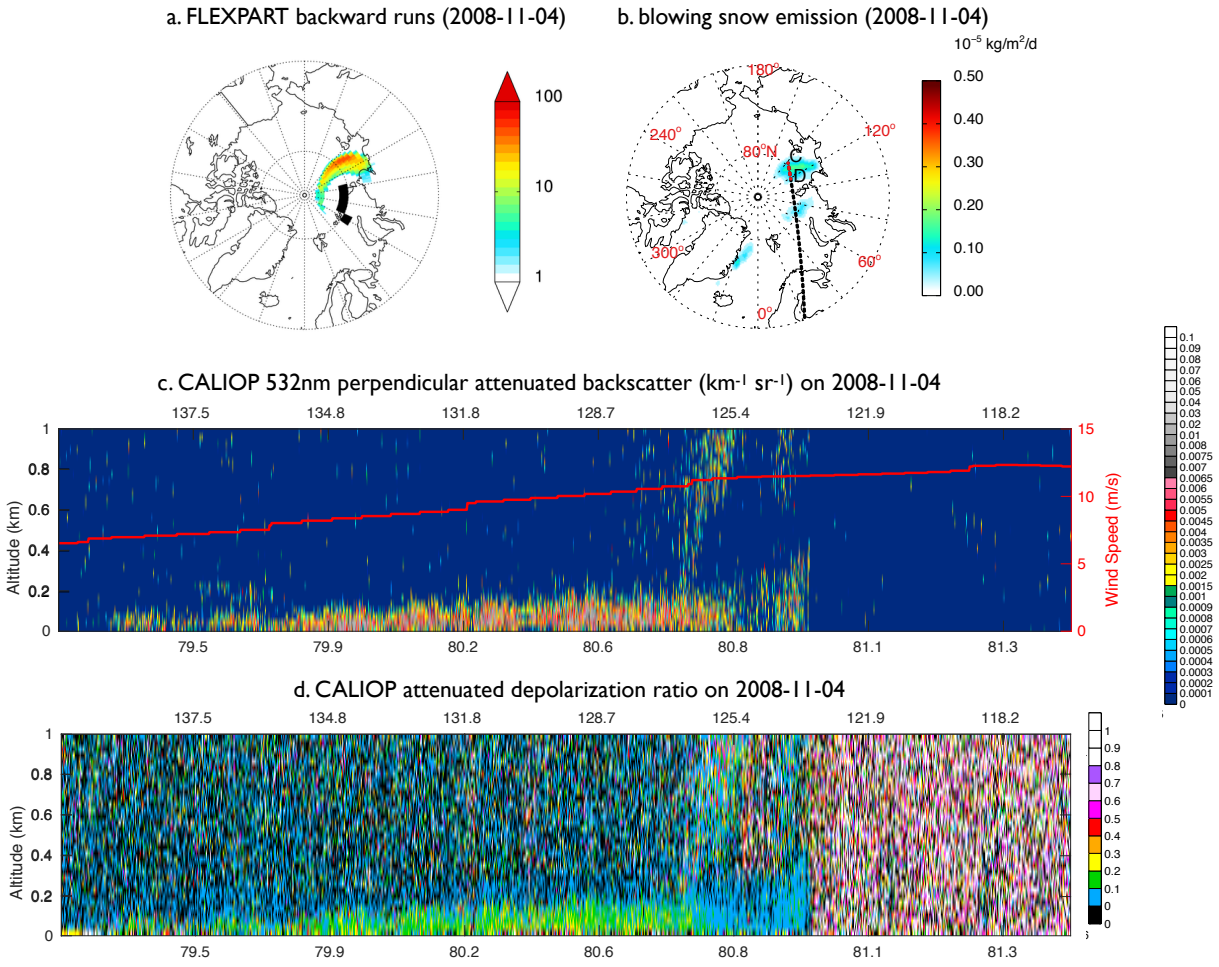

Figure 2.8. (a) The November 4, 2008 FLEXPART footprint below 100m (in seconds) for particles initialized at 0-2 km over the black squares on November 6, 2008, near the blowing snow feature

observed by CALIOP (Figure 2.7). (b) November 4, 2008 blowing snow SSA emissions from the STD+Snow simulation, and the CALIOP overpass at 01:11–01:24 UTC on that day. The bottom two panels display CALIOP cross-sections between points C and D for (c) the 532nm perpendicular attenuated backscatter (km^{-1} sr^{-1}) and (d) attenuated depolarization ratio. The surface wind speeds (m s^{-1}) are shown with a red line in panel c.

2.6 Discussion and conclusions

In this work, we used the GEOS-Chem chemical transport model to assess the ability of the CALIOP Lidar onboard the CALIPSO satellite to provide constraints on sea ice sources of SSA. We find that mean CALIOP aerosol extinction coefficients below 2 km altitude reach 10–15 Mm^{-1} over sea ice covered regions during the 6-month polar cold season. The enhanced extinctions are located below 2 km, with the largest values (20–35 Mm^{-1}) occurring near the surface. We find that a standard GEOS-Chem simulation without sea ice sources of SSA underestimates CALIOP extinctions by 50–70% over Arctic and Antarctic sea ice. A simulation with frost flower SSA emissions is unable to explain the spatial and temporal distribution of CALIOP aerosol extinctions. Adding a blowing snow SSA source results in improved agreement over the Arctic (NMB = –7% for first year sea ice (FYI) and +17% over multi-year sea ice (MYI)), but yields a 43% overestimate of CALIOP extinctions over Antarctic sea ice. Additionally, the simulation including blowing snow SSA tends to underestimate CALIOP observations during fall–early winter (October–December over the Arctic and April over the Antarctic).

We hypothesize that our assumption of constant surface snow salinity on FYI (0.1 psu over the Arctic and 0.03 psu over the Antarctic) in the blowing snow simulation could explain this underestimate. Given the paucity of snow salinity observations, we infer the monthly surface snow salinity on FYI required to minimize the discrepancy between CALIOP extinctions and the GEOS-Chem simulation. The resulting snow salinities decrease progressively between the beginning and end of the cold season (from 0.9 to 0.09 psu for Arctic FYI; 0.05 to 0.018 psu over Antarctic FYI). This decrease is consistent with the seasonally increasing sea ice thickness and accumulating snow depth. The optimized blowing snow model using the monthly-varying snow salinities shows improved agreement with CALIOP observations and in situ observations of SSA mass concentrations at five surface sites. However, the optimized blowing snow model tends to underestimate the aerosol extinctions over the Canadian Arctic Archipelago and off the Ross Ice-shelf. Both regions are predicted to favor frost flower growth, which could locally increase the salinity of snow when frost flowers are buried under snow. We find that increasing the Canadian Arctic Archipelago FYI snow salinity to 3 psu would help reconcile our simulation with CALIOP and in situ observations. Our work, however, cannot rule out other alternative factors contributing to the discrepancy between modeled and observed aerosol extinctions, such as the impact of the negative feedback of water vapor sublimation and our assumption of the number of particle produced per snowflake. Systematic observations of surface snow salinity over multiple sea ice locations and times would help further constrain snow salinities in the Arctic and Antarctic. Furthermore, more extensive observations of sea salt aerosol size distributions during blowing snow events, can help further refine and constraint these assumptions.

We conduct a case study of a blowing snow SSA event over the Arctic which was detected by CALIOP on November 6, 2008 and predicted by our blowing snow simulation. Using FLEXPART, we find that the observed aerosol extinction layer originated 2 days earlier over sea ice below 100m altitude. We demonstrate that CALIOP detects this blowing snow event with enhanced extinction below 200 m and large depolarization ratio, co-located with surface high winds.

Our work suggests that blowing snow emissions are the dominant source of SSA over sea ice covered regions during cold months. As SSA can act as a source of halogens, inclusion of blowing snow in chemical transport models is important to understand springtime bromine explosions and the resulting ozone and mercury depletion events (Schroeder et al., 1998; Simpson et al., 2007; Steffen et al., 2008; Gilman et al., 2010; Yang et al., 2010). Furthermore, these sea-ice sources of SSA can act as ice nuclei for cloud formation, and may increase the downward longwave radiative forcing (Xu et al., 2013). Arctic sea ice has been rapidly changing over the past 30 years, with decreasing sea ice extent and thickness (e.g. Kwok and Rothrock, 2009), a shift towards less MYI and more FYI (Fowler et al., 2004; Maslanik et al., 2007), and a thinning of snow depth in spring (Renner et al., 2014; Blanchard-Wrigglesworth et al., 2015). All these factors are likely to have resulted in an increase in snow salinity on sea ice, and hence increasing SSA emissions from blowing snow. In the Southern Hemisphere, sea ice extent is FYI-dominant, and it annual/seasonal trend is more complex, varying in space. Sea ice extent has been increasing over the Ross Sea, but decreasing over the Amundsen-Bellingshausen Sea over the past decades (Turner et al., 2009; Parkinson and Cavalieri, 2012; Stammerjohn et al., 2012). Consequently, this may have resulted in a shift in the spatial pattern of blowing snow SSA

emissions, with increased influence over the Ross Sea and reduced influence over the Amundsen-Bellingshausen Sea.

CHAPTER 3

EVALUATING THE IMPACT OF BLOWING SNOW EMISSIONS ON SPRINGTIME TROPOSPHERIC BRO AND O_3 OVER THE ARCTIC

This Chapter is in preparation for submission for publication.

Abstract

We use the GEOS-Chem chemical transport model to examine the influence of bromine release from blowing snow sea salt aerosol (SSA) on springtime Arctic composition. We evaluate our simulation against comparisons to tropospheric BrO columns from the GOME-2 and OMI spaceborne instruments for three years (2007-2009). We find that inclusion of blowing snow SSA results in a factor of 4-10 enhancement in tropospheric BrO columns in March-April, similar to the enhancements observed GOME-2 and OMI. We find that the inclusion of halogen release from blowing snow SSA is necessary to capture the timing and locations of observed BrO explosion events over the springtime Arctic. We calculate that the blowing snow simulation captures 56% of the BrO explosion events. However, the simulation only reproduces 20–30% of the ODEs over the springtime Arctic. This underestimate in the occurrence and magnitude of ODEs could be related either to surface snow chemistry or to chloride release from blowing snow SSA which are processes that are do not currently taken into account. We estimate that inclusion of halogen chemistry from blowing snow SSA increases Br_y abundance by a factor of 2.6 below 2 km altitude during spring (March−May), and decreases boundary layer O_3 by 10% (0.61 DU) on average. We find that the influence of blowing snow SSA on O_3 extends to the northern midlatitudes, where surface O_3 decreases by 2% (0.14 DU).

3.1 Introduction

Ozone depletion events (ODEs) near the surface are often observed over the springtime Arctic (Bottenheim et al., 1986; Oltmans and Komhyr, 1986, Barrie et al., 1988; Bottenheim and Chan, 2006; Bottenheim et al., 2009; Koo et al., 2012; Oltmans et al., 2012; Halfacre et al., 2014). While ODEs occur episodically at coastal Arctic sites, lasting 1-3 days, they are more persistent and widespread over the frozen ocean (e.g. Simpson et al., 2007 and references therein). These ODEs have been linked to the release of significant levels of bromine radicals, in a phenomenon called bromine explosion (Simpson et al., 2007; Abbatt et al., 2012). Both ground-based and satellite instruments have reported elevated concentrations of BrO during March and April (Hönninger and Platt, 2002; Wagner et al., 2001; Jones et al., 2009; Neuman et al., 2010; Salawitch et al., 2010; Theys et al., 2011; Liao et al., 2012; Peterson et al., 2017; Simpson et al., 2017; Choi et al., 2012, 2018). An autocatalytic cycle involving the heterogeneous release of bromide (Br^-) via uptake of HOBr was suggested to be the primary cause of bromine explosion and ODEs (Hausmann and Platt, 1994; Fan and Jacob, 1992, Simpson et al., 2007; Abbatt et al., 2012):

$$HOBr + Br^- + H^+ \longrightarrow H_2O + Br_2 \quad (1)$$

$$Br_2 + hv \longrightarrow 2Br \quad (2)$$

$$Br + O_3 \longrightarrow BrO + O_2 \quad (3)$$

$$BrO + HO_2 \longrightarrow HOBr + O_2 \quad (4)$$

The sources of enhanced bromine radicals over springtime Arctic, however, remain poorly understood. In the global troposphere, inorganic bromine (Br_y) has three major sources:

debromination of sea salt aerosols (SSA) which are produced by breaking waves in the open ocean; photolysis and oxidation of bromocarbons; and transport from stratosphere. Production of bromide content in oceanic SSA is estimated to be 1.4-6.2 Tg/yr, and is the largest source of tropospheric bromine (Sander et al, 2003; Parrella et al., 2012). Current global chemical models that include these three sources of tropospheric bromine, however, cannot reproduce the observed elevated levels of tropospheric BrO over polar regions (Theys et al., 2011, Parrella et al., 2012; Schmidt et al., 2016). Several substrates have been proposed as sources of Br^- in reaction (1) specific to polar regions: SSA produced from frost flowers, SSA produced from blowing snow, salty snowpack on sea ice, and coastal regions (Oum et al, 1998; Rankin et al, 2002; Yang et al., 2008; Pratt et al, 2013). Laboratory experiments conducted by Oum et al. (1998) showed that frozen seawater can release gas-phase Br_2 in the presence of O_3. Rankin et al. (2002) reported that Br^- concentrations in frost flowers were a factor of 4–5 higher than those in seawater, and could thus contribute to the Arctic ODEs once activated and released. Using forward trajectories, Kaleschke et al. (2004) suggested that satellite observations of bromine explosions are associated with newly-formed sea ice where frost flowers are likely to grow. This was disputed by Simpson et al. (2007), who showed that the BrO abundance over Barrow, Alaska, is unrelated to air mass in contact with frost flower formation regions, but is instead related to contact with first-year sea ice. They proposed that sea-salt-contaminated snow and ice over first-year sea ice regions are the main Br^- source over polar regions. Yang et al. (2008, 2010) proposed blowing snow SSA, produced after sublimation of wind-lofted salty snow on sea ice, as a source of bromine. Theys et al. (2011) showed two examples of satellite observations of bromine explosions that were qualitatively reproduced by blowing snow SSA in the p-TOMCAT model. In outdoor chamber experiments, Pratt et al. (2013) reported Br_2 production when

acidified surface saline snow was exposed to sunlight. However, no Br_2 was detected over sea ice and brine icicles, suggesting that brines and frost flowers are unlikely to be a direct source of reactive bromine.

In this study, we examine the role of blowing snow SSA in springtime Arctic bromine explosions and the associated tropospheric O_3 loss using the GEOS-Chem chemical transport model. We evaluate our 3-year simulation (2007-2009) via comparisons to satellite retrievals of tropospheric BrO columns from the second Global Ozone Monitoring Experiment (GOME-2) and the Ozone Monitoring Instrument (OMI), as well as in situ observations of O_3 at two Arctic sites (Barrow, Alaska; Alert, Nunavut, Canada). The GEOS-Chem model is described in section 2. In section 3, we evaluate GEOS-Chem's capability in reproducing the observed GOME-2 and OMI bromine explosion events. In section 4, we examine the simulation of ODEs at Alert and Barrow. In section 5, we quantify the impact of blowing snow SSA on BrO and O_3 abundance over the Arctic and mid-latitudes.

3.2 Observations

The Second Global Ozone Monitoring Experiment (GOME-2) is a nadir-scanning UV/visible spectrometer on the METOP-A satellite, which was launched on October 19, 2006 in a sun-synchronous polar orbit with an equator crossing time of 9:30 LT (Munro et al., 2006). GOME-2 is an ultraviolet/visible spectrometer covering 240−790 nm with a spectral resolution between 0.26 and 0.51 nm. It has a ground pixel size of 80 km × 40 km, and a scanning swath of 1920 km that enables global coverage within 1.5 days. In this study, we use the daily 2007-2009 GOME-2 tropospheric BrO columns retrieved by Theys et al. (2011). Briefly, the tropospheric BrO

columns are derived from a residual technique that combines measured slant columns and calculated stratospheric columns, accounting for the impact of clouds, surface reflectivity and viewing geometry on the measurement sensitivity. The stratospheric BrO contribution is removed using the dynamic climatology based on the BASCOE CTM as described in Theys et al., (2009, 2011). In this work, we regrid the daily 80 km × 40 km tropospheric BrO column densities to a horizontal resolution of 4°× 5° for comparison to GEOS-Chem.

We also use tropospheric BrO columns from the Ozone Monitoring Instrument (OMI) onboard the Aura satellite launched on July 15, 2004 in a sun-synchonous polar orbit with a 13:30 LT equator overpass time (Levelt et al., 2006). OMI is a nadir solar backscatter spectrometer that measures ultraviolet–visible wavelengths (270–500 nm), and has a horizontal resolution of 13 km × 14 km and swath width of 2600 km. Since 2008, the OMI swath coverage has been reduced due to an external obstruction. We use here the daily 2007-2009 tropospheric BrO columns retrieved by Choi et al (2018) for the months of March and April. The OMI tropospheric BrO columns are retrieved using the residual technique and the dynamic climatology stratospheric BrO columns from Theys et al. (2011). The total BrO slant column densities are derived from OMI total bromine monoxide (OMBRO) product, by fitting a model function to OMI UV backscattered radiance at 319–347.5 nm (Choi et al., 2018). In this work, we regrid the OMI tropospheric column densities to 4°× 5°.

We also use hourly O_3 observed at Barrow, Alaska (71.3ºN, 156.6ºW); and Alert, Nunavut, Canada (82.5ºN, 62.5ºW). The observations from these surface monitoring sites are obtained

through the World Data Center for Greenhouse Gases (WDCGG; http://ds.data.jma.go.jp/gmd/wdcgg/) from the World Meteorological Organization (WMO) Global Atmospheric Watch (GAW).

3.3 The GEOS-Chem chemical transport model

GEOS-Chem is a 3-D global chemical transport model (Bey et al., 2001). In this work, we use GEOS-Chem v11-02, driven by the Modern-Era Retrospective analysis for Research and Applications, version 2 (MERRA-2) assimilated meteorological fields (Gelaro et al., 2017), which have a native horizontal resolution of 0.5º latitude by 0.625º longitude with 72 vertical levels. We regrid the MERRA-2 fields to a 4º× 5º horizontal resolution and 47 vertical levels with merged levels above 80 hPa for computational expediency.

GEOS-Chem includes detailed HO_x-NO_x-VOC-O_3-halogen-aerosol tropospheric chemistry. The chemical mechanism in GEOS-Chem v11-2 was updated to the most recent JPL/IUPAC recommendations, with recent updates described in (Fischer et al., 2014; Fischer et al., 2016; Mao et al., 2013; Travis et al., 2016). A new feature as part of this version of GEOS-Chem is the inclusion of detailed bromine-chlorine-iodine halogen chemistry. The bromine chemistry mechanism was first described in Parrella et al. (2012). The bromine chemistry scheme was updated by Schmidt et al. (2016) to include extensive multiphase chemistry, as well as coupling to tropospheric chlorine chemistry, which provides an important pathway to recycle bromine radicals. The uptake coefficient of heterogeneous reaction between HOBr, $ClNO_3$ and O_3 with Br^-, as well as reaction of HOBr with Cl^- aerosol particles follows Ammann et al. (2013). The

uptake coefficient between O_3 and Br^- takes into account both bulk and surface reactions. Sherwen et al. (2016ab) implemented iodine chemistry and Cl-Br-I interactions. Chen et al. (2017) added the in-cloud oxidation of dissolved SO_2 (S(IV)) by HOBr in GEOS-Chem, which decreased the global Br_y burden by 50% and resulted in improved agreement with GOME-2 tropospheric BrO columns between 60ºN and 60ºS. Fifteen bromine tracers are transported in GEOS-Chem (Br_2, Br, BrO, HOBr, HBr, $BrNO_2$, BrCl, $BrONO_2$, $CHBr_3$, CH_2Br_2, CH_3Br, IBr, CH_2IBr, Br^- on submicron SSA and Br^- on supermicron SSA) with sources from photolysis of $CHBr_3$, oxidation of $CHBr_3$, CH_2Br_2 and CH_3Br by OH radicals, transport of reactive bromine from the stratosphere, and SSA debromination.

Open ocean emissions of SSA are a function of wind speed and sea surface temperature (SST) as described in Jaeglé et al. (2011), with updates from Huang and Jaeglé (2017) for cold ocean waters (SST < 5°C). The blowing snow SSA simulation is described in Huang and Jaeglé (2017) and Huang et al. (2018). Blowing snow SSA emissions are a function of relative humidity, temperature, age of snow, surface snow salinity and wind speeds following the parameterizations of Yang et al. (2008, 2010). For surface snow on Arctic first-year sea-ice, we use monthly-varying salinity (0.9 to 0.09 practical salinity unit (psu, parts per thousand)) based on comparisons to CALIPSO aerosol extinctions, while for snow on Arctic multi-year sea ice we assume a salinity of 0.01 psu (Huang et al., 2018). The empirically derived surface snow salinities lead to an overall improved model performance in simulating the surface SSA mass concentrations and aerosol extinction coefficients over the Arctic, but the model tends to underestimate the aerosol extinctions over the Canadian Arctic Archipelago Huang et al., (2018) proposed that increasing the surface snow salinity over Canadian Arctic Archipelago to 3

psu can help reconcile the model discrepancy and suggested that snow-covered frost flowers in that region could increase the local surface snow salinity. In this study, we assume the salinity of surface snow over the Canadian Arctic Archipelago (defined as the region between 65-80ºN and 80-130ºW) to be 3 psu. As in Huang and Jaeglé (2017), we assume N=5 for number of SSA particles produced per snowflake, and a mean snow age of 3 days over the Arctic. Two size bins for SSA are used in the model: accumulation mode (r_{dry} = 0.01−0.5 μm) and coarse mode (r_{dry} = 0.5–8 μm).

For open-ocean SSA, we assume a bromide to chloride (Br^-/Cl^-) molar ratio of 1/647, based on seawater composition. In surface snow measurements on sea ice near Alert, Domine et al. (2004) report that Br^- was enriched by factors of 5 relative to seawater, while surface snow over a Northern Arctic Ocean site further away displayed a factor of 32 enrichment in Br^-. Sampling conducted by Pratt et al. (2013) near Barrow, Alaska shows Br^- enrichment factors of 7 for surface snow on sea ice. In surface snow samples over Antarctic sea ice, Maffezzoli et al. (2017) report Br^- enrichment factors of 2-10 with a median of 5.7. The reasons for these Br^- enrichments in snow are unclear, but could be due to the precipitation of hydrohalite ($NaCl\text{-}2H_2O$) below 251K in brine (Abbatt et al., 2013) as well as to atmospheric aerosol and trace gas deposition onto surface snow (Simpson et al., 2007; Pratt et al., 2013). Contamination by frost flowers may also contribute to Br^- enrichment in surface snow. Frost flowers collected from the Barne Glacier, Antarctica have Br^-/Cl^- ratios of 1/347 to 1/269 at about –35°C, with enrichment factors of 2-3 (Kalnajs and Avallone, 2006). Morin et al. (2008) conducted a model study simulating the evolution of Br^-/Cl^- ratios in frost flowers, and found that it increases up to

1/100 at –43°C. In our simulation, we assume a Br^- enrichment factor of 10 for blowing snow SSA for both multi-year and first-year sea ice and a factor of 5 for the region near Alert.

Global anthropogenic emissions are from EDGAR v4.2 (Olivier and Berdowski, 2001) for 1970-2008. Biomass burning emissions are from Global Fire Emissions Database version 4 (GFEDv4) emission inventory, which is based on burned area, active fire detections and plant productivity with constraints from satellite observations (van der Werf et al., 2010). Dust emissions are based on the dust entrainment and deposition scheme from Zender et al. (2003). Biogenic emissions of volatile organic compounds (VOCs) are from the Model of Emissions of Gases and Aerosols from Nature version 2.1 (MEGAN 2.1, Guenther et al., 2012).

In this study, we first conduct a 2007-2009 halogen-oxidant-aerosol simulation in which the only source of SSA is from wave breaking in the open ocean. We will refer to this as our standard simulation (STD). In a second simulation, we add SSA produced from blowing snow (STD+SNOW). Both simulations are initialized with a 1-year spin up in 2006.

For comparison with the GOME-2 satellite observations of BrO, we sampled the model outputs at LT 11:00-20:00 over the Arctic. The model is sampled at the dates and locations of GOME-2 overpasses where tropospheric BrO column densities retrievals are available.

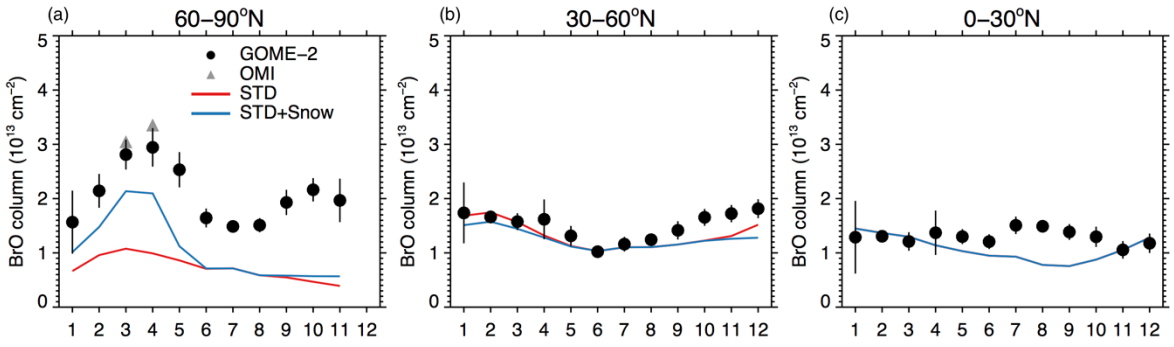

Figure 3.1. Seasonal variation of 2007-2009 monthly mean tropospheric BrO column densities (10^{13} molecules cm^{-2}) as observed by GOME-2 satellite (black circles), as well as calculated with the GEOS-Chem standard simulation (STD, red line) and blowing snow simulation (STD+Snow, blue line) in the northern hemisphere over the Arctic (>60°N) (a), mid-latitudes (30–60°N) (b) and the tropics (0–30°N) (c). Also shown in (a) are the April and May tropospheric BrO column densities retrieved from the OMI satellite (gray triangles).

Previous GEOS-Chem model versions have also been evaluated against GOME-2 BrO tropospheric column densities (Schmidt et al., 2016; Sherwen et al., 2016a; Chen et al., 2017). Schmidt et al. (2016) showed that the inclusion of SSA debromination resulted in a 50-100% overestimate in BrO in the northern hemisphere. Sherwen et al. (2016b) added iodine chemistry and disabled SSA debromination, finding relatively good agreement with GOME-2 observations over the Arctic and the summertime low- and mid- latitudes. Chen et al. (2017) added in-cloud oxidation of dissolved S(IV) with HOBr to the model version of Schmidt et al. (2016) without iodine chemistry. They found improved agreement with GOME-2 tropospheric BrO columns over low- and mid- latitudes, but a factor of 3-10 underestimate over high latitudes (Chen et al., 2017). Our STD version of GEOS-Chem includes SSA debromination, the in-cloud oxidation of dissolved S(IV) by HOBr, as well as iodine chemistry, and simple chlorine chemistry. Figure

3.1bc shows that, by including these three components, the STD simulation agrees well with the GOME-2 tropospheric BrO columns at 0–60°N. Over the Arctic (>60°N), the STD simulation underestimates both GOME-2 and OMI observations by factors of 2–5. Addition of blowing snow SSA (STD+Snow) leads to improved agreement between January and April over the Arctic, but the BrO underestimate remains unchanged for other months.

3.4 Comparison between modeled and observed tropospheric BrO and surface ozone over the Arctic

3.4.1 Monthly mean Arctic tropospheric BrO columns

The GOME-2 tropospheric BrO columns display springtime (March−April) maxima of about 3×10^{13} molecules cm^{-2} over the Arctic (60−90°N) in 2007−2009 (Figure. 3.1a), with most of the enhancement taking place over the sea ice covered Arctic Ocean. The OMI tropospheric BrO column densities during March−April are in good agreement with those in GOME-2, with OMI being higher by 10% in March and 15% in April on average (Figure. 3.1a). The STD model does not capture this springtime maxima and simulates tropospheric BrO column densities up to only $\sim1\times10^{13}$ molecules/cm^2. The inclusion of blowing snow SSA emissions in the STD+Snow simulation doubles the simulated springtime tropospheric BrO column concentrations and reproduces the timing and magnitude of the observed springtime BrO enhancement (Figure. 3.1a).

GOME-2 tropospheric BrO columns show a secondary maxima in October−November reaching $\sim2.1\times10^{13}$ molecules/cm^2. This is caused in part by the seasonal variations of GOME-2 spatial

coverage. While the swath of GOME-2 reaches up to 90°N in April−September, it only reaches up to 75°N in October and 65°N in November. We find that the secondary maxima of BrO in October−November is due to elevated tropospheric BrO column densities over the Eurasian continents in a narrow latitude band between 60 and 70°N. This fall maxima is not reproduced by GEOS-Chem.

We note that in June-August, when sea ice extent is at its minimum and blowing snow SSA emissions are small, GEOS-Chem underestimates GOME-2 tropospheric BrO columns by a factor of 2. This underestimate of background BrO levels might be due to the fact that we do not consider acid displacement of HCl from SSA (Schmidit et al, 2016). Over the cloudy Arctic, the reaction HOBr+S(IV) provides a sink for HOBr, and decreases the Br_y abundance by about 70−90% (Chen et al., 2017). We hypothesize that including this source of HCl from SSA would lead to a competition between HOBr reacting with Cl^- and S(IV) in cloud droplets, and thus increase the HOBr levels. For the rest of this discussion, we focus on the observed and simulated Arctic springtime tropospheric BrO column enhancement (ΔBrO) relative to summer months. The ΔBrO is defined as the enhancement above the corresponding summer mean values in each gridbox.

Figure 3.2 shows the spatial distributions of tropospheric ΔBrO column densities during March and April 2007−2009. In March, both GOME-2 and OMI show enhanced ΔBrO columns (up to 5×10^{13} molecules/cm^2) over the Canadian Arctic Archipelago and central Arctic ocean (Figure. 2ab). In April, the observed ΔBrO reaches 3×10^{13} molecules/cm^2 over the Eastern Arctic Ocean (Figure. 3.2ef). GOME-2 and OMI show similar distributions for ΔBrO, with OMI columns

being 10-15% higher than GOME-2. The STD simulation predicts ΔBrO columns generally less than 1×10^{13} molecules/cm^2 in March-April (Figure. 3.2cg). The STD+Snow simulation appears to successfully reproduce the spatial distribution and magnitude of the satellite retrievals of ΔBrO in March, with the largest enhancements over the Canadian Arctic Archipelago extending to the central Arctic Ocean, with smaller enhancements in Baffin Bay and the Greenland Sea (Figure. 3.2dh). While GOME-2 and OMI show that elevated ΔBrO extends inland over the Russian Arctic coast, in the STD+Snow simulation the enhancement is mostly restricted over the Arctic Ocean. For April, the STD+Snow simulation shows that most of the BrO enhancement is over the central Arctic Ocean.

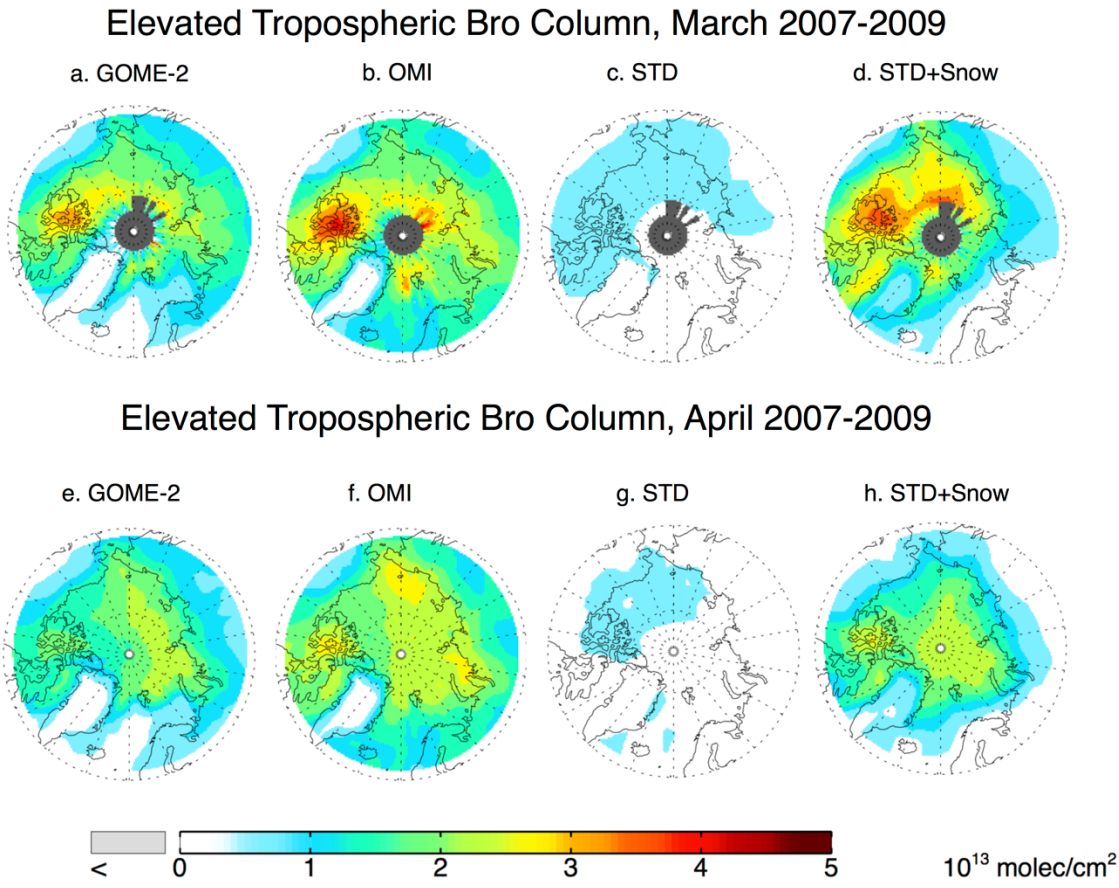

Figure 3.2. Spatial distribution of ΔBrO tropospheric column densities (enhancement above June-August mean columns) in March (top row) and April (bottom row) 2007–2009. Satellite retrievals from GOME-2 (panels a and e) and OMI (panels b and f) are compared to the GEOS-Chem standard simulation (STD, panels c and g) and blowing snow simulation (STD+Snow, panels d and h).

3.4.2 Daily tropospheric BrO column

As discussed in previous studies (Theys et al., 2011; Nghiem et al., 2012; Choi et al., 2018) satellite observations show the frequent occurrence of BrO explosion events over the Arctic sea ice. Here, we define a BrO explosion event as the region where daily tropospheric BrO columns exceed the 10^{th} percentile over the high Arctic (>64°N) in March−April in 2007−2009. For GOME-2 this threshold is 4.66×10^{13} molecules/cm^2, for OMI it is slightly higher (5.18×10^{13} molecules/cm^2), while in the GEOS-Chem STD+Snow simulation it is 4.0×10^{13} molecules/cm^2. We use these respective thresholds to calculate the daily area covered by BrO explosion events. Figure 3a shows the timeseries of the total area (km^2) where BrO explosion events occur, and Figure 3b shows the timeseries of total SSA burden at >64°N.

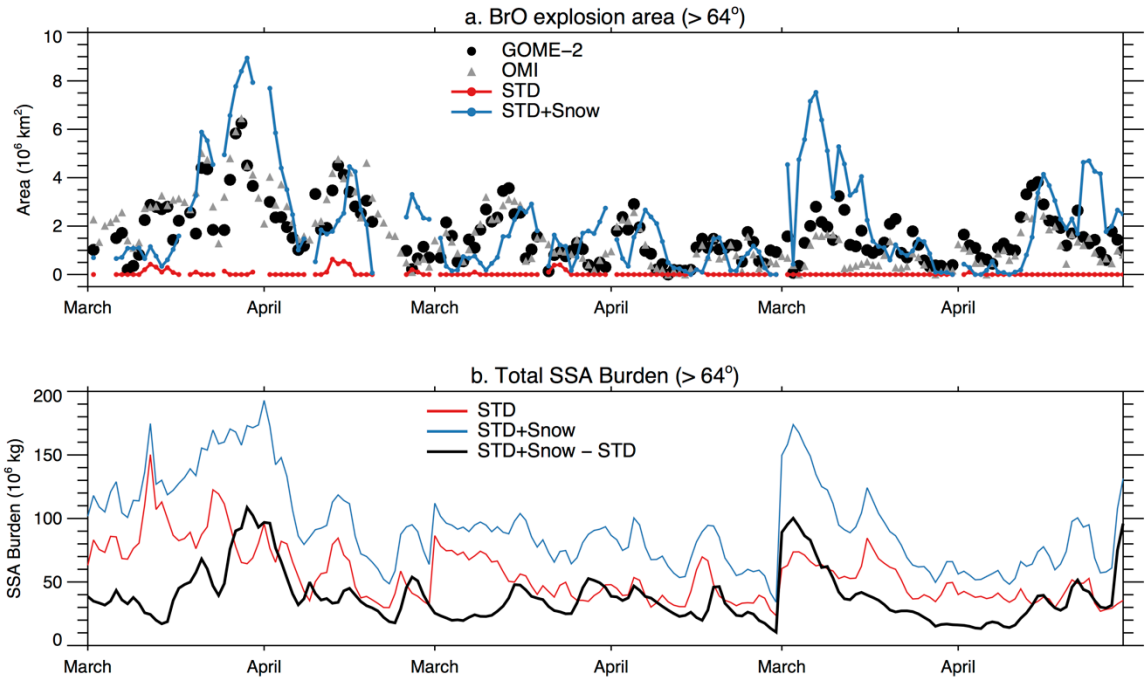

Figure 3.3 The timeseries of total area coverage where BrO explosion events occur (a), as well as the total SSA burden over high latitudes (>65°N) (b) during March−April in 2007−2009. In (a), black circles are GOME-2 observations and gray triangles are from OMI observations. Model results are shown in dotted red line (STD model) and blue line (STD+Snow model). Panel (b) shows the total SSA burden in STD (red line) and STD+Snow (blue line). Black lines indicates the SSA burden contributed by blowing snow emission alone.

GOME-2 and OMI show similar results in terms of spatial coverage of BrO explosion events and their variability (Figure. 33.a). Typically, BrO explosion events reach maximum extents of 1-6.5×10^6 km^2. Focusing only on events reaching extents greater than 10^6 km^2, we see that they last between several days to 2 weeks. The largest of the BrO explosion events observed by GOME-2 and OMI occurs in late March 2007. The STD+Snow simulation reproduces the overall observed day-to-day variations in spatial coverage of BrO explosions, often capturing the

timing of the large events. We find that this variability is driven by the temporal variations in the blowing snow SSA burden (Figure. 3.3b). We assume that a BrO explosion occurs when the mean GOME-2 and OMI daily area extent exceeds 1×10^6 km^2. We find that 61% of the days in March-April 2007-2009 fit this definition. The STD+Snow simulation is within 30% of the observed extent on 21% of those days, and overestimates the observed extent by >30% on 48% of those days.

As noted above, the largest bromine explosion in 2007-2009 occurred between March 26−30, 2007. This BrO explosion event is reproduced by the blowing snow model, and some of the largest blowing snow SSA burdens are predicted during this event (Figure. 3.3ab).

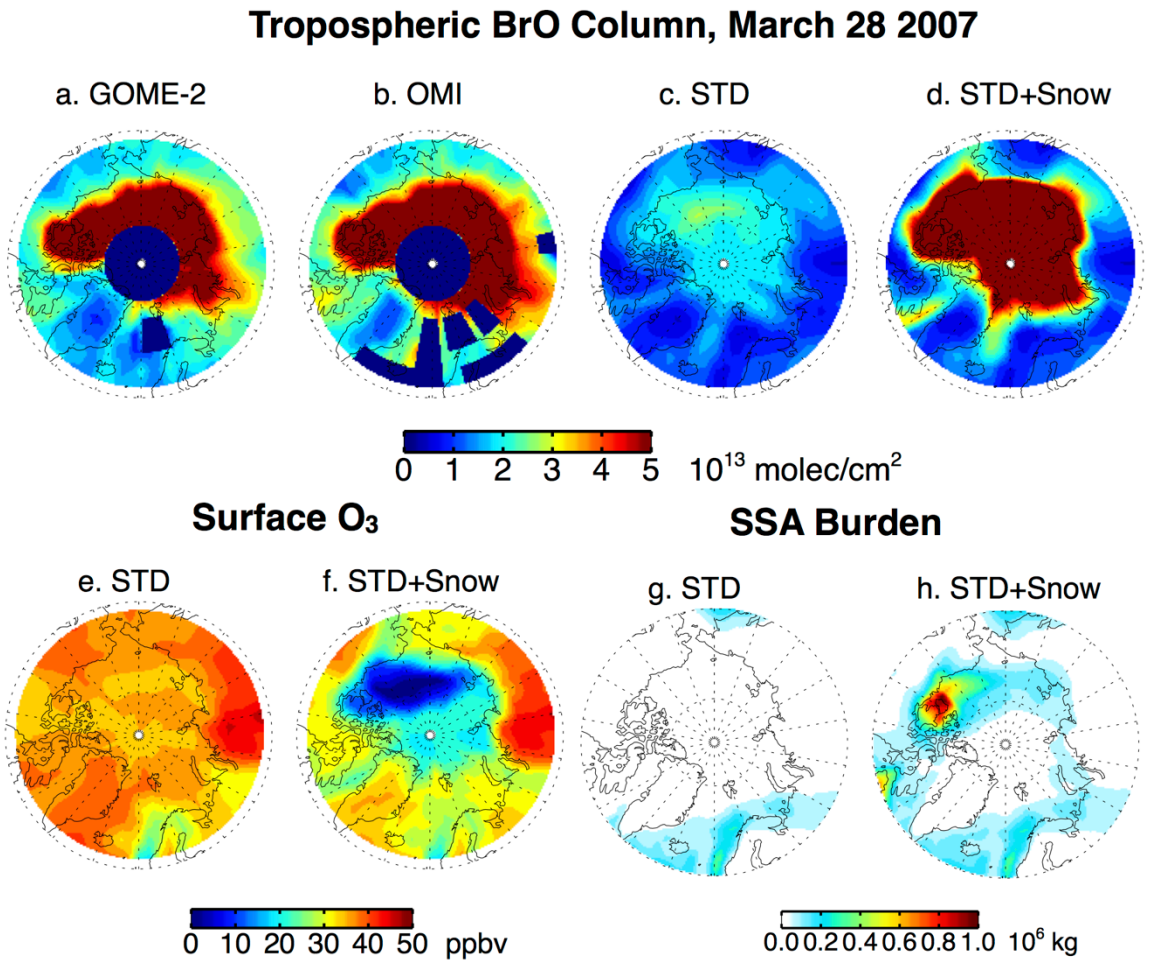

Figure 3.4. Top row: March 28, 2007 distribution of tropospheric BrO columns for GOME-2, OMI and the GEOS-Chem model simulations (STD and STD+Snow). Bottom row: Surface ozone concentrations (ppbv) in the standard (STD) and blowing snow (STD+Snow) simulations on March 28, 2007 (panels e and f). Also shown are the SSA burden (units of 10^6 kg) in the STD model (h) and STD+Snow (i) simulations. The dark blue areas in panels a and b correspond to regions with no BrO retrievals. Note that polar sunrise occurred equatorward of 80°N.

Figure 3.4 (top panels) shows the observed and modeled spatial distributions of tropospheric BrO columns on March 28, 2007, which is day 3 of this extensive BrO explosion event. The GOME-2 and OMI tropospheric BrO columns concentrations exceed 5×10^{13} molecules/cm^2 over the sea-ice covered region in the high Arctic region (>70°N) on March 28, 2007 (Figure. 3.4ab). The STD+Snow reproduces both the magnitude and spatial distribution this BrO explosion event. The elevated BrO levels over Arctic sea ice is attributed to the debromination of SSA from blowing snow emissions over the Beaufort Sea and Canadian Archipelago (Figure. 3.4gh). This particular BrO explosion event was also previously discussed in Begoin et al. (2010) and Choi et al. (2018). Using the FLEXPART model, Begoin et al. (2010) linked this event to a cyclone with very high surface wind speeds, which is favorable for blowing snow events or lifting aerosols. Choi et al. (2018) found that the spatial pattern of OMI tropospheric BrO column during this BrO explosion event was consistent with that of the GEOS-5 simulated blowing snow SSA burden.

During this BrO explosion event, the STD+Snow simulation shows that surface O_3 concentrations reach very low levels (0−10 ppbv) over the Beaufort Sea and the East Siberian Sea, and are generally around 20 ppbv over the rest of the Arctic Ocean (Figure. 3.4f). Relative to the fairly uniform surface O_3 concentrations of 35-40 ppbv in the STD simulation, the STD+Snow model predicts that during this event blowing snow resulted in the depletion of 50-100% of surface O_3.

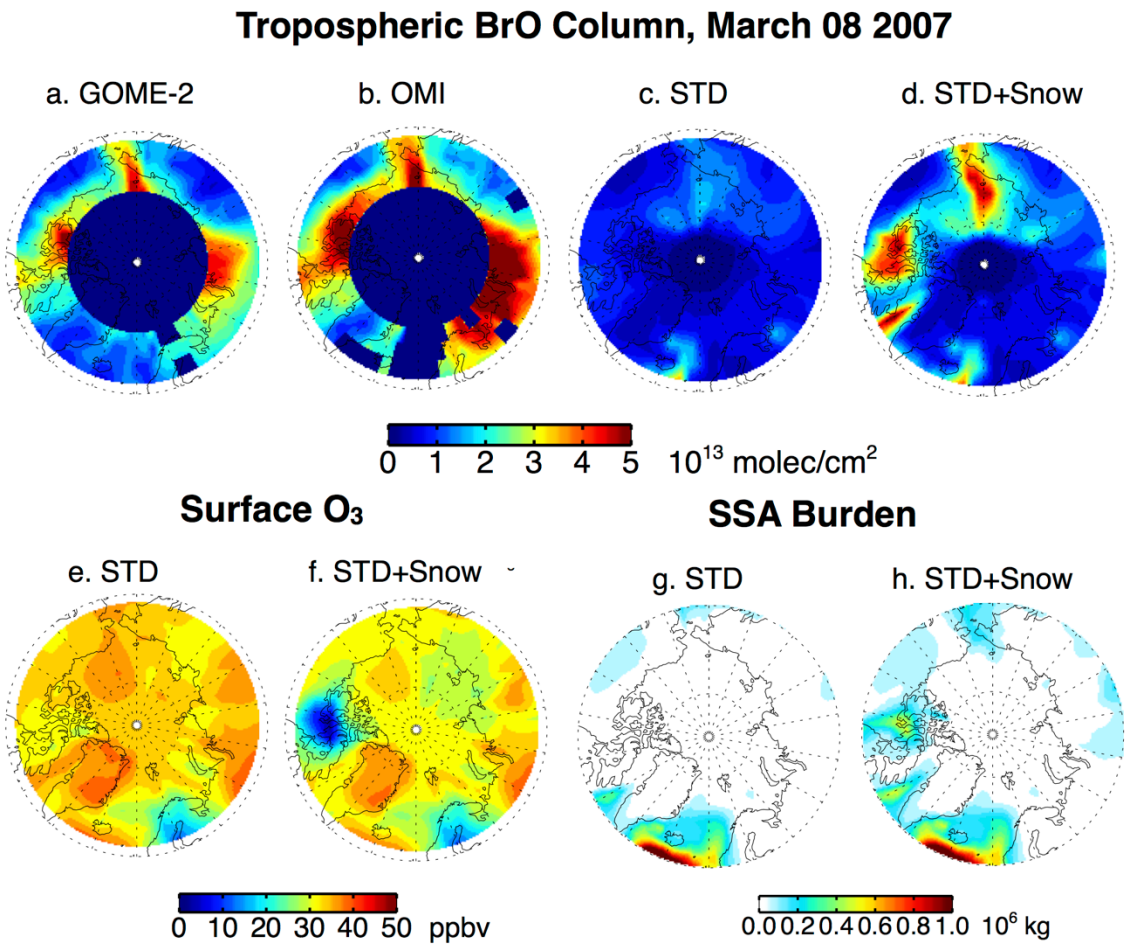

Figure 3.5 Same as Figure 3.4, but for March 08, 2007.

In addition to this large extensive BrO explosion event, the blowing snow model is also capable of capturing the BrO explosion events in relatively smaller spatial extent, such as the one on March 08, 2007 (Fig 5). Both GOME-2 and OMI observations shows enhanced tropospheric BrO levels over sea ice covered region in Beaufort Sea, Chukchi Sea, as well as the Russian continent. The blowing snow model capture the spatial distribution and magnitudes of the tropospheric BrO enhancements over the Beaufort Sea and Chukchi Sea, although it fails to capture the enhanced BrO levels over the Russian continents.

3.4.3 Model evaluation with in-situ surface O_3 observations

Figures 3.6a and 3.7a show the timeseries of observed and modeled surface O_3 at Alert, Nunavut, Canada and Barrow, Alaska, USA for the year 2007. Also shown are the modeled vertical distribution of O_3 and BrO mixing ratios at these two sites.

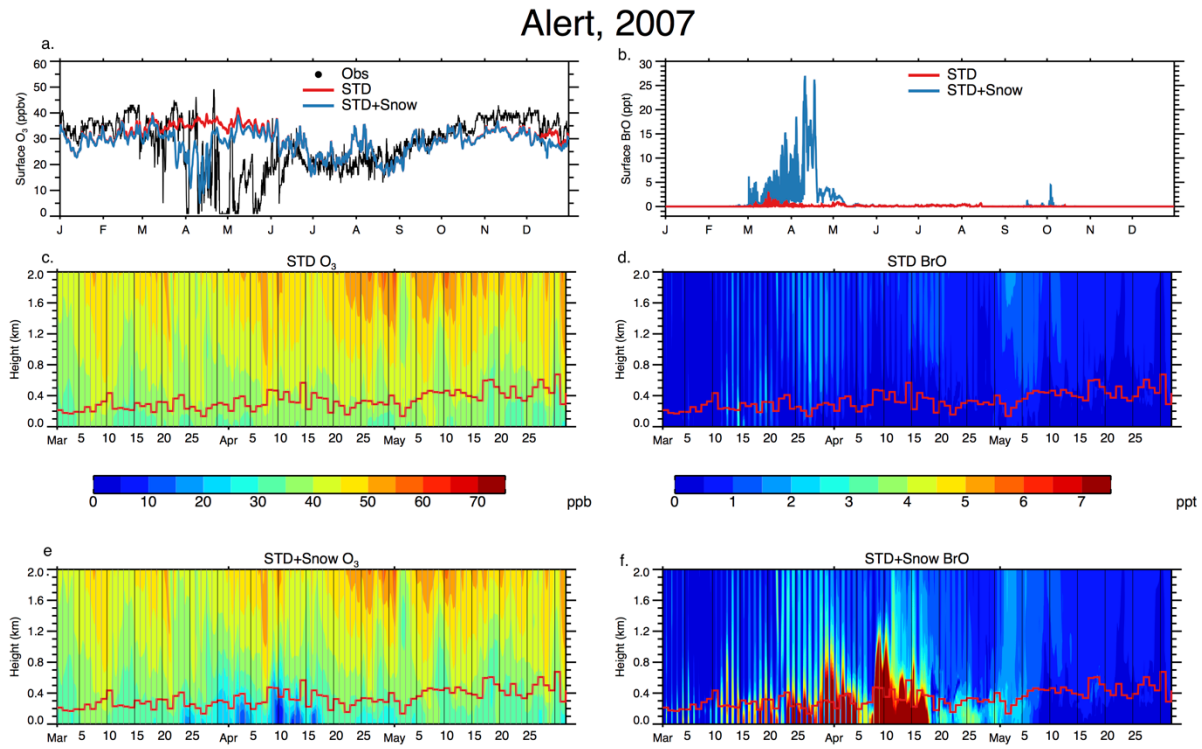

Figure 3.6 (a) Timeseries of hourly surface O_3 (ppbv) at Alert, Nunavut, Canada for the year 2007: in situ observations (black line), GEOS-Chem STD simulation (red line) and STD+Snow simulation (blue line). (b) Timeseries of modeled hourly surface BrO (pptv) at Alert. Also shown are the time-height cross-sections of O_3 (c, e) and BrO (d, f) in the STD and STD+Snow simulations between March 1 and May 31 2007. The red line indicates the boundary layer height.

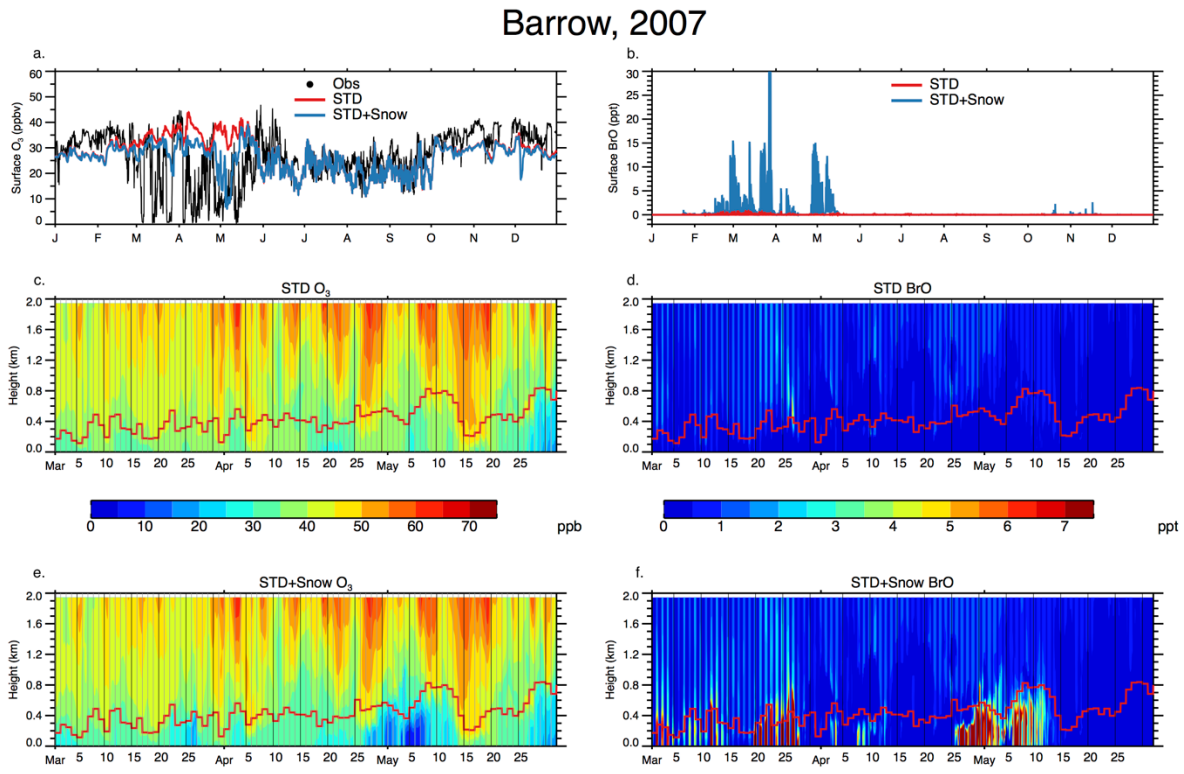

Figure 3.7. Same as Figure 3.6, but for Barrow, Alaska in 2007.

ODEs occurred frequently at Alert and Barrow during March−May 2007 (Figure. 3.6a and 3.7a). While the simulated surface O_3 concentration in the STD model is generally in good agreement with the observations during June−February, the simulated surface O_3 varies between 28−42 ppbv during March−May, failing to capture the observed ODEs. Inclusion of blowing snow emissions leads to very small changes in the surface O_3 levels at both sites during winter in absence of sunlight. During the Arctic spring (March−May), the STD+Snow simulation show enhanced surface BrO concentrations of 5-30 pptv. At Alert, the STD+Snow simulation captures the timing and magnitude of some of the observed ODEs at Alert, in particular between March 10-April 10, 2007, but does not reproduce the ODEs observed between late April and late May (Figure. 6a). At Barrow, the situation is reversed and the STD+Snow simulation does not

reproduce the early spring ODEs (March 1-April 15), but does capture the timing and magnitude of ODEs for April 27−May 9, 2007 (Figure. 3.7a). We define ODEs as times when surface O_3 decreases by more than 1 ppb per hour. The observations capture ~9 days of ODEs in 2007. We calculate the fraction of ODEs captured by the STD+Snow simulation as times when the simulated surface O_3 decreases by more than 0.1 ppb per hour. With this definition, we find that the STD+Snow simulation captures 30% of the observed ODEs at Alert, and 21% at Barrow during March−May 2007.

In the STD+Snow simulation, the inclusion of blowing snow emissions decreases the springtime O_3 by up to 40 ppbv at Alert and Barrow, and its impact on O_3 is most significant within the boundary layer, below 500 m altitude (Figure. 3.6ce and 3.7ce). The increases in BrO abundance caused by blowing snow emission are also largest within the boundary layer, although the influence of blowing snow emissions on BrO and O_3 can extend up to 2 km at Alert and 1 km at Barrow (Figure. 3.6df and 3.7df).

3.5 The impact of blowing snow emissions on the Arctic burden of Br_y and ozone burden

Table 3.1 summarizes the simulated March-May 2007-2009 Br_y and O_3 burdens for three regions: northern hemisphere (0–90°N), Arctic (>60 °N) and mid-latitudes (30−60°N). We find that blowing snow SSA has the largest impact on the Br_y abundance below 2 km altitude, increasing the Br_y abundance by a factor of 2.6 over the Arctic. In particular, the BrO abundance below 2 km over the Artic increases from 0.06 Gg Br in the STD model to 0.27 Gg Br in the STD+Snow model, and HOBr increases from 0.05 Gg Br to 0.09 Gg Br. The percentage changes

of bromine species caused by blowing snow emissions range from +800% for Br atoms to +25% for HBr.

	Br_y 0−90°N (Gg Br)	**Bry >60°N (Gg Br)**	**Bry 30−60°N (Gg Br)**	**O_3 0−90°N (DU)**	**O_3 >60°N (DU)**	**O_3 30−60°N (DU)**
Total troposphere						
STD	16.3	1.26	5.98	32.3	26.96	35.82
STD+Snow	17.1	1.87	6.16	31.9	26.04	35.57
Diff	+0.8	+0.61	+0.18	−0.4	−0.92	−0.25
0−2 km						
STD	5.6	0.33	1.85	6.19	6.92	6.78
STD+Snow	6.25	0.85	2.0	5.93	6.31	6.64
Diff	+0.65	+0.52	+0.15	−0.26	−0.61	−0.14

Table 3.1. Summary of Br_y burden (Gg Br) and ozone burden (DU) over northern hemisphere (0−90°N), over high latitudes (>60°N) and mid-latitudes (30−60°N) as simulated in the standard model (STD) and blowing snow model (STD+Snow). The "diff" indicates the difference between blowing snow model and standard model (=STD+Snow – STD).

Figure 3.8 shows the changes in the Br_y and O_3 burdens due to blowing snow SSA. We find that the impact of bromine release from blowing snow SSA on Br_y abundance is largest over the Canadian Archipelago and the Beaufort Sea, consistent with where blowing snow SSA is most abundant (Figure. 8). The influence of blowing snow is not limited to the Arctic Ocean, it extends to land regions over Eurasia and North America, down to 45°N.

Halogen chemistry from blowing snow SSA decreases the tropospheric O_3 columns by ~1% over the northern hemisphere and mid-latitudes and ~4% over the high latitudes. Below 2 km, the

blowing snow SSA lead to a 10% decreases in the ozone levels over the Arctic and ~5% decreases in the northern hemisphere (0–90°N). The spatial distribution of O_3 changes is consistent with the spatial distribution for changes in Br_y abundance, but extends more broadly down to 30°N due to the longer lifetime of O_3 (Figure. 3.8).

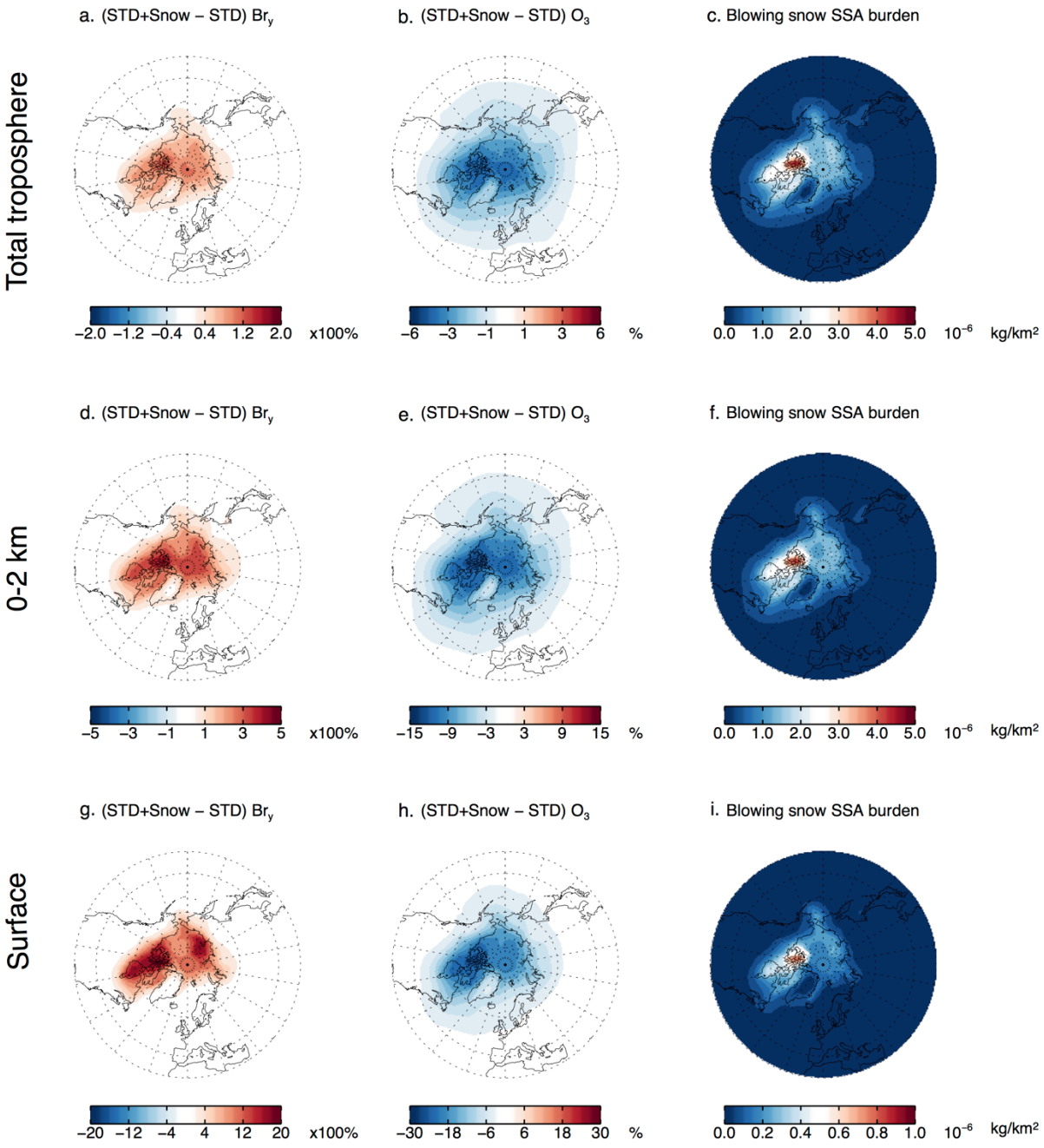

Figure 3.8. Spatial distributions of mean percentage changes of Br_y burdens ($\times 100\%$) and O_3 burdens (%), as well as the absolute values of SSA burdens (kg/km^2) at >30°N during March−May in 2007−2009 in the total troposphere (a−c), 0−2 km (d−f) and at the surface (g−i). Note the different colorbars used for each panel.

3.6 Discussion and conclusions

We used the GEOS-Chem model to examine the impact of SSA from blowing snow on bromine chemistry and O_3. We evaluated our simulation against comparison to satellite observations of tropospheric BrO columns from GOME-2 and OMI for 2007-2009. The background levels of BrO in GEOS-Chem is generally lower than those in the GOME-2 and OMI satellite observations poleward of 60°N, but the model captures the broad increase in tropospheric BrO columns observed in March and April. Focusing on the BrO column enhancements above background, we find that the blowing snow GEOS-Chem simulation can capture both the timing and magnitude of the BrO explosions observed by GOME-2 and OMI. The blowing snow model is able to reproduce the day-to-day variations of the observed total area coverage of BrO explosion events at >65°N, and is able to capture 56% of the BrO explosion events. The simulated surface ozone mixing ratio in the blowing snow model also agrees well with the in-situ observations during the extensive ozone depletions events at Alert, Nunavut, Canada on April 8−10, 2007 and at Barrow, Alaska on April 27−May 9, 2007. However, the blowing snow model cannot capture all of the ozone depletion events and underestimates the magnitude of some ODEs in the observations. We estimate that blowing snow model captures 21−30% of the ODEs at Alert and Barrow during March–May 2007. This underestimate in O_3 loss might reflect the fact that we do not consider acid displacement of Cl^- in SSA. Such a release of Cl^-, would further

enhance O_3 loss. Indeed interactions between bromine, chlorine, and iodine chemistry have been shown to significantly enhance the rate of O_3 depletion (e.g., Thompson et al., 2015) In addition, the Br^- enrichment factor for the surface snow on sea ice is poorly constrained with handful in-situ measurements. Therefore, the time and spatial dependence of the Br^- concentrations in surface snow are not considered here. Also, surface snow chemistry is not considered in this study, which may provide additional source for the bromine in the Arctic boundary layer.

In previous modeling studies, Yang et al. (2010) and Theys et al. (2011) used depletion factors to calculate the bromine release from blowing snow SSA in the p-Tomcat model, and found similarities in the modeled and observed BrO explosions in terms of time and locations. However, the spatial comparisons between model and observations in their studies are limited to 1 single month (March 1998 in Yang et al. (2010) and April 2008 in Theys et al. (2011)) over the Arctic, and the model discrepancies are relatively large.

The influence of surface snow chemistry in examined in Falk and Sinnhuber (2018) by implementing the surface snow bromine chemistry via assigning molar yields for bromine release based on surface types and illumination in the EMAC model. Falk and Sinnhuber (2018) found that the bromine release from surface snowpack can help explain the temporal variations of surface O_3 to some extent. Falk and Sinnhuber (2018) also compared total BrO vertical column densities in GOME and the EMAC model in April 2000, and found consistent enhanced BrO levels over the Canadian Arctic Archipelago. However, their estimates of BrO explosion events may be disguised by stratospheric BrO variance (Falk and Sinnhuber, 2018)

In our simulation, we find that bromine generated by blowing snow SSA enhances Br_y by a factor of 2.6 in the Arctic boundary layer (0−2 km) during spring (March−May), and results in a 10% mean decreases in boundary layer O_3 concentrations.

Our model results rely on simplifying assumptions about surface snow Br^- enrichment factors and salinity. Therefore, extensive observations of surface snow salinities and Br− at various time and locations will be extremely helpful to further constrain our simple assumptions in the model and improve our understanding of the role of blowing snow.

Chapter 4.

CONCLUSIONS AND FUTURE WORK

In Chapter 2, observations of aerosol extinction from the Cloud-Aerosol Lidar with Orthogonal Polarization (CALIOP) were used to constrain SSA emissions from blowing snow and frost flowers within the GEOS-Chem chemical transport model. While the standard model underestimated the aerosol extinctions over Arctic and Antarctic sea ice by 50–70%, inclusion of blowing snow emissions decreased the model discrepancies to –7% to +17% over Arctic sea ice and to +43% over Antarctic sea ice. We found that frost flowers cannot explain the observed spatial and temporal distribution of CALIOP aerosol extinctions. We hypothesized that the remaining model discrepancy with CALIOP observations is due to our assumption of constant surface snow salinities (=0.1 psu over the Arctic and 0.03 psu over the Antarctic) in the blowing snow emissions scheme, and derived monthly varying salinity of surface snow on first year sea ice. We found that surface snow salinity on first year sea ice progressively decreases between the beginning and end of the cold season. The blowing snow model using the monthly-varying snow salinities shows improved agreement with both the CALIOP aerosol extinctions and in-situ mass concentrations at polar sites. We also conducted a case study demonstrating that CALIOP can detect an Arctic blowing snow event occurred on November 6, 2008 as well as the resulting enhanced aerosol extinction coefficients, and its time and locations are consistent with the prediction of the blowing snow model using the monthly-varying snow salinities.

In Chapter 3, we used the monthly-varying snow salinities derived in Chapter 2 to calculate blowing snow emission of SSA in the model, and implemented bromine release from blowing snow SSA. Following the field measurements and experiments of Br– in the surface snow, sea

ice and frost flower in the previous studies, we assumed that surface snow is enriched in Br– by a factor of 5-10 compared to seawater. We find that the blowing snow model can capture both the timing and magnitude of BrO explosion events as observed in the Second Global Ozone Monitoring Experiment (GOME-2) and the Ozone Monitoring Instrument (OMI). In addition, the blowing snow model can capture some of the springtime surface ozone depletion events observed at the Barrow and Alert ground-sites. The Arctic boundary layers receive largest influence of blowing snow emissions on BrO and ozone concentrations. Inclusion of blowing snow emissions increases the Arctic (>60°N) Br_y burden below 1 km by a factor of 4, and decrease the Arctic ozone burden below 1km by 13%.

Recommendations for future work

The modeling study in my Ph.D. project suggests that blowing snow emissions are a dominant source of SSA over the polar regions during cold months. As Arctic sea ice has been changing rapidly over the past 30 years, we can expect changes in the sea ice properties (such as shifting toward less multi-year sea ice and more first year sea ice, and thinning of snow depth). These changes in sea ice properties could potentially increase surface snow salinity, and consequently increase the blowing snow emissions of SSA. As SSA can act as cloud condensation nuclei for cloud formation, these additional blowing snow sources of SSA may increase the downward longwave radiative forcing (Xu et al., 2013). Therefore, it would be useful to include blowing snow SSA in a climate model to evaluate its radiative impact and how this impact evolves with the changing polar climate.

The uncertainty in parametrizations of blowing snow emissions is in part due to limited observations of surface snow salinity on sea ice. The spatial and temporal variation of surface snow salinity are critical to estimates of blowing snow SSA emissions. Systematic observations of surface snow salinities at various time and locations could thus be extremely helpful to further refine blowing snow SSA emissions.

In this work, the number of particles produced per snowflake is assumed to be 5 in the blowing snow scheme based on the partitioning of submicron and supermicron SSA mass concentrations at Barrow, Alaska. Although this number has a small influence on the total blowing snow emissions, it is critical to determine the size distribution of blowing snow SSA. However, this number is poorly constrained. Detailed observations of the size distributions of snow particles and SSA during blowing snow events would be very helpful to constrain this number.

The age of surface snow is assumed to be 3 days over the Arctic and 1.5 over the Antarctic sea ice based on the calculation of MERRA meteorological fields. The younger snow is more easily lifted by winds, and thus increases blowing snow SSA emissions. We made a simple assumption of constant snow age in this work. Online calculation of surface snow age can provide a more accurate estimate of blowing snow emissions.

In my Ph.D. project, I focused on the halogen chemistry from blowing snow over the Arctic. Over the Antarctic, the tropospheric BrO column densities are underestimated by ~70% all year round in the model. The inclusion of blowing snow emission leads to relatively small improvement. In the clean southern ocean environment, SSA can serve as the main source of cloud condensation nuclei, and therefore the modeled in-cloud Cl^- concentrations calculated via liquid-gas partitioning of HCl may be underestimated in this region. This can lead to

overestimate of in-cloud reaction between HOBr with S(IV) which provides a sink for HOBr. Currently, Cl^- concentration in cloud or aerosols is not a tracer in the GEOS-Chem. Implementation of Cl^- as a tracer for online calculation of in-cloud and aerosol Cl^- would be necessary to address this issue.

The model study presented here suggests that activation of bromine from blowing snow SSA is critical to understand the BrO explosions and ozone depletion events over the springtime Arctic. In this work, our simulation only captures 20–30% of the observed surface ODEs at Barrow and Alert. The remaining model discrepancy may be related to surface snow photochemical chemistry. which release Br_2 from local snow surfaces and leads to ODEs (Pratt et al., 2013; Falk and Sinnhuber, 2018). Comparing and coupling the influence of blowing snow emissions and surface snow chemistry will be of great interest, and will provide important insights for the halogen chemistry in the polar regions. It could also be that release of chloride from SSA would further enhance the rate of ozone depletion. Inclusion of this process in GEOS-Chem and examining its coupling to bromine chemistry would be useful.

Reactive halogen species oxidize elemental mercury to reactive mercury which then gets deposited to sea ice and snow surface in mercury depletions events (Ariya et al., 2004; Simpson et al., 2007). It would be very interesting in couple the new SSA blowing snow scheme with the GEOS-Chem mercury simulation to examine whether the model can capture observed mercury depletion events. Such a simulation would allow to assess how much mercury is deposited to the fragile polar ecosystems.

The uncertainty in estimating the halogen release from blowing snow SSA mainly comes from the poorly constrained Br– contents in the blowing snow SSA due to limited observations. In this

project, I use the Br– contents estimated based on handful measurements of Br–/Cl– ratios in surface snow and frost flowers. More systematic observations of the Br– content in the surface snow and lofted blowing snow particles can be very useful to refine the assumptions used in the model.

Chapter 5.

BIBLIOGRAPHY

Abbatt, J. P. D., Thomas, J. L., Abrahamsson, K., Boxe, C., Granfors, A., Jones, A. E., King, M. D., Saiz-Lopez, A., Shepson, P. B., Sodeau, J., Toohey, D. W., Toubin, C., von Glasow, R., Wren, S. N., and Yang, X.: Halogen activation via interactions with environmental ice and snow in the polar lower troposphere and other regions, Atmos. Chem. Phys., 12, 6237-6271, doi:10.5194/acp-12-6237-2012, 2012.

Abram, N. J., Wolff, E. W., and Curran, M. A. J.: A review of sea ice proxy information from polar ice cores, Quaternary Sci. Rev., 79, 168–183, doi:10.1016/j.quascirev.2013.01.011, 2013.

Alvarez-Aviles, L., Simpson, W. R., Douglas, T. A., Sturm, M., Perovich, D., and Domine, F.: Frost flower chemical composition during growth and its implications for aerosol production and bromine activation, J. Geophys. Res., 113, D21304, doi:10.1029/2008JD010277, 2008.

Ammann, M., Cox, R. A., Crowley, J. N., Jenkin, M. E., Mellouki, A., Rossi, M. J., Troe, J., and Wallington, T. J.: Evaluated kinetic and photochemical data for atmospheric chemistry: Volume VI – heterogeneous reactions with liquid substrates, Atmos. Chem. Phys., 13, 8045-8228, https://doi.org/10.5194/acp-13-8045-2013, 2013.

Ariya, P., Dastoor, A. P., Amyot, M., Schroeder, W. H., Barrie, L., Anlauf, K., Raofie, F., Ryzhkov, A., Davignon, D., Lalonde, J., and Steffen, A.: The Arctic: a sink for mercury, Tellus, 56B, 397–403, 2004.

Barber, D. G., Reddan, S. P., and Ledrew, E. F.: Statistical Characterization of the Geophysical and Electrical-Properties of Snow on Landfast First-Year Sea-Ice, J. Geophys. Res.-Oceans, 100, 2673–2686, doi:10.1029/94jc02200, 1995.

Barrie, L. A., Bottenheim, J. W., Schnell, R. C., Crutzen, P. J., and Rasmussen, R. A.: Ozone destruction and photochemical reac- tions at polar sunrise in the lower Arctic atmosphere, Nature, 334, 138–141, 1988.

Begoin, M., Richter, A., Weber, M., Kaleschke, L., Tian-Kunze, X., Stohl, A., Theys, N., and Burrows, J. P.: Satellite observations of long range transport of a large BrO plume in the Arctic, Atmos. Chem. Phys., 10, 6515-6526, https://doi.org/10.5194/acp-10-6515-2010, 2010.

Bey, I., Jacob, D. J., Yantosca, R. M., Logan, J. A., Field, B. D., Fiore, A. M., Li, Q., Liu, H. Y., Mickley, L. J., and Schultz, M. G.: Global modeling of tropospheric chemistry with assimilated meteorology: Model description and evaluation, J. Geophys. Res.-Atmos., 106, 23073–23095, doi:10.1029/2001jd000807, 2001.

Blanchard-Wrigglesworth, E., Farrell, S.L., Newman, T. and Bitz, C.M.: Snow cover on Arctic sea ice in observations and an Earth System Model. Geo. Res. Lett., 42(23), 10,342–10,348, doi:10.1002/2015GL066049, 2015.

Bond, T. C., Bhardwaj, E., Dong, R., Jogani, R., Jung, S. K., Roden, C., Streets, D. G., and Trautmann, N. M.: Historical emissions of black and organic carbon aerosol from energy-

related combustion, 1850–2000, Global Biogeochem. Cy., 21, GB2018, doi:10.1029/2006gb002840, 2007.

Bottenheim, J., Gallant, A.G. and Brice, K.A. Measurements of NOy species and O3 at 82 N latitude. Geophysical Research Letters, 13(2), pp.113-116, 1986.

Bottenheim, J. W., Netcheva, S., Morin, S., and Nghiem, S. V.: Ozone in the boundary layer air over the Arctic Ocean: measurements during the TARA transpolar drift 2006–2008, Atmos. Chem. Phys., 9, 4545-4557, https://doi.org/10.5194/acp-9-4545-2009, 2009.

Bottenheim, J. W. and Chan, E.: A trajectory study into the origin of spring time Arctic boundary layer ozone depletion, J. Geophys. Res., 111, D19301, doi:10.1029/2006JD007055, 2006.

Chen, Q., Schmidt, J. A., Shah, V., Jaeglé, L., Sherwen, T., and Alexander, B.: Sulfate production by reactive bromine: Implica- tions for the global sulfur and reactive bromine budgets, Geophys. Res. Lett., 44, 7069–7078, 2017.

Choi, S., Wang, Y., Salawitch, R. J., Canty, T., Joiner, J., Zeng, T., Kurosu, T. P., Chance, K., Richter, A., Huey, L. G., Liao, J., Neu- man, J. A., Nowak, J. B., Dibb, J. E., Weinheimer, A. J., Diskin, G., Ryerson, T. B., da Silva, A., Curry, J., Kinnison, D., Tilmes, S., and Levelt, P. F.: Analysis of satellite-derived Arctic tropo- spheric BrO columns in conjunction with aircraft measurements during ARCTAS and ARCPAC, Atmos. Chem. Phys., 12, 1255– 1285, https://doi.org/10.5194/acp-12-1255-2012, 2012.

Choi, S., Theys, N., Salawitch, R.J., Wales, P.A., Joiner, J., Canty, T.P., Chance, K., Suleiman, R.M., Palm, S.P., Cullather, R.I. and Darmenov, A.S.: Link Between Arctic Tropospheric BrO Explosion Observed From Space and Sea-Salt Aerosols From Blowing Snow Investigated Using Ozone Monitoring Instrument BrO Data and GEOS-5 Data

Assimilation System. Journal of Geophysical Research: Atmospheres, 123(13), pp.6954-6983, 2018.

de Leeuw, G., Andreas, E. L., Anguelova, M. D., Fairall, C. W., Lewis, E. R., O'Dowd, C., Schulz, M., and Schwartz, S. E.: Production flux of sea-spray aerosol, Rev. Geophys., 49, RG2001, doi:10.1029/2010RG000349, 2011.

Di Pierro, M., Jaeglé, L., Eloranta, E. W., and Sharma, S.: Spatial and seasonal distribution of Arctic aerosols observed by the CALIOP satellite instrument (2006–2012), Atmos. Chem. Phys., 13, 7075-7095, doi:10.5194/acp-13-7075-2013, 2013.

Domine, F., Sparapani, R., Ianniello, A., and Beine, H. J.: The origin of sea salt in snow on Arctic sea ice and in coastal regions, Atmos. Chem. Phys., 4, 2259-2271, doi:10.5194/acp-4-2259-2004, 2004.

Domine, F., Taillandier, A. S., Simpson, W. R., and Severin, K.: Specific surface area, density and microstructure of frost flowers, Geophys. Res. Lett., 32, L13502, doi:10.1029/2005GL023245, 2005.

Falk, S. and Sinnhuber, B.-M.: Polar boundary layer bromine explosion and ozone depletion events in the chemistry–climate model EMAC v2.52: implementation and evaluation of AirSnow algorithm, Geosci. Model Dev., 11, 1115-1131, https://doi.org/10.5194/gmd-11-1115-2018, 2018.

Fan, S.M. and Jacob, D.J.: Surface ozone depletion in Arctic spring sustained by bromine. Nature, 359, p.8, 1992.

Fischer, H., Siggaard-Andersen, M.L., Ruth, U., Röthlisberger, R., and Wolff, E.: Glacial/interglacial changes in mineral dust and sea-salt records in polar ice cores: Sources, transport, and deposition, Rev. Geophys., 45, RG1002, doi:10.1029/2005rg000192, 2007.

Fisher, J.A., D.J. Jacob, A.L. Soerensen, H.M. Amos, E.S. Corbitt, D.G. Streets, Q. Wang, R.M. Yantosca, and E.M. Sunderland, Factors driving mercury variability in the Arctic atmosphere and ocean over the past thirty years, Global Biogeochem. Cycles, 27, 1226-1235, 2013.

Fisher, J.A., D.J. Jacob, K.R. Travis, P.S. Kim, E.A. Marais, C. Chan Miller, K. Yu, L. Zhu, R.M. Yantosca, M.P. Sulprizio, J. Mao, P.O. Wennberg, J.D. Crounse, A.P. Teng, T.B. Nguyen, J.M. St. Clair, R.C. Cohen, P. Romer, B.A. Nault, P.J. Wooldridge, J.L. Jimenez, P. Campuzano-Jost, D.A. Day, P.B. Shepson, F. Xiong, D.R. Blake, A.H. Goldstein, P.K. Misztal, T.F. Hanisco, G.M. Wolfe, T.B. Ryerson, A. Wisthaler, and T. Mikoviny. Organic nitrate chemistry and its implications for nitrogen budgets in an isoprene- and monoterpene-rich atmosphere: constraints from aircraft (SEAC4RS) and ground-based (SOAS) observations in the Southeast US. Atmos. Chem. Phys., 16, 2961-2990, 2016.

Fisher, J.A., L.T. Murray, D.B.A. Jones, and N.M. Deutscher, Improved method for linear carbon monoxide simulation and source attribution in atmospheric chemistry models illustrated using GEOS-Chem v9, Geosci. Model Dev., 10, 4129-4144, 2017.

Fountoukis, C. and Nenes, A.: ISORROPIA II: a computationally efficient thermodynamic equilibrium model for K+–Ca2+–Mg2+–NH4+–Na+–SO42−–NO3−–Cl−–H2O aerosols, Atmos. Chem. Phys., 7, 4639-4659, doi:10.5194/acp-7-4639-2007, 2007.

Fowler, C., Emery, W. J., Maslanik, J.: Satellite-derived evolution of Arctic sea ice age: October 1978 to March 2003. IEEE Geosci Remote Sens Soc Lett 1(2):71–74, doi:10.1109/LGRS.2004.824741, 2004.

Gelaro, R., McCarty, W., Suárez, M.J., Todling, R., Molod, A., Takacs, L., Randles, C.A., Darmenov, A., Bosilovich, M.G., Reichle, R. and Wargan, K.: The modern-era

retrospective analysis for research and applications, version 2 (MERRA-2). Journal of Climate, 30(14), pp.5419-5454, doi:10.1175/JCLI-D-16-0758.1, 2017.

Geldsetzer, T., Langlois, A., and Yackel, J.: Dielectric properties of brine-wetted snow on first-year sea ice, Cold Re.g. Sci. Technol., 58, 47–56, doi:10.1016/j.coldregions.2009.03.009, 2009.

Gilman, J. B., Burkhart, J. F., Lerner, B. M., Williams, E. J., Kuster, W. C., Goldan, P. D., Murphy, P. C., Warneke, C., Fowler, C., Montzka, S. A., Miller, B. R., Miller, L., Oltmans, S. J., Ryerson, T. B., Cooper, O. R., Stohl, A., and de Gouw, J. A.: Ozone variability and halogen oxidation within the Arctic and sub-Arctic springtime boundary layer, Atmos. Chem. Phys., 10, 10223-10236, doi:10.5194/acp-10-10223-2010, 2010.

Guenther, A. B., Jiang, X., Heald, C. L., Sakulyanontvittaya, T., Duhl, T., Emmons, L. K., and Wang, X.: The Model of Emissions of Gases and Aerosols from Nature version 2.1 (MEGAN2.1): an extended and updated framework for modeling biogenic emissions, Geosci. Model Dev., 5, 1471-1492, doi:10.5194/gmd-5-1471-2012, 2012.

Halfacre, J. W., Knepp, T. N., Shepson, P. B., Thompson, C. R., Pratt, K. A., Li, B., Peterson, P. K., Walsh, S. J., Simpson, W. R., Matrai, P. A., Bottenheim, J. W., Netcheva, S., Perovich, D. K., and Richter, A.: Temporal and spatial characteristics of ozone depletion events from measurements in the Arctic, Atmos. Chem. Phys., 14, 4875-4894, https://doi.org/10.5194/acp-14-4875-2014, 2014.

Hara, K., Osada, K., Yabuki, M., and Yamanouchi, T.: Seasonal variation of fractionated sea-salt particles on the Antarctic coast, Geophys. Res. Lett., 39, L18801, doi:10.1029/2012GL052761, 2012.

Hara, K., Matoba, S., Hirabayashi, M., and Yamasaki, T.: Frost flowers and sea-salt aerosols over seasonal sea-ice areas in northwestern Greenland during winter–spring, Atmos. Chem. Phys., 17, 8577-8598, doi:10.5194/acp-17-8577-2017, 2017.

Hausmann, M. and Platt, U.: Spectroscopic measurement of bromine oxide and ozone in the high Arctic during Po- lar Sunrise Experiment 1992, J. Geophys. Res., 99, 25399, doi:10.1029/94JD01314, 1994.

Hönninger, G. and Platt, U.: Observations of BrO and its vertical distribution during surface ozone depletion at Alert. Atmospheric Environment, 36(15), pp.2481-2489, 2002.

Huang, J. and Jaeglé, L.: Wintertime enhancements of sea salt aerosol in polar regions consistent with a sea ice source from blowing snow, Atmos. Chem. Phys., 17, 3699-3712, doi:10.5194/acp-17-3699-2017, 2017.

Huang, J., Jaeglé, L., and Shah, V.: Using CALIOP to constrain blowing snow emissions of sea salt aerosols over Arctic and Antarctic sea ice, Atmos. Chem. Phys. Discuss., doi:10.5194/acp-2018-298, in review, 2018.

Jacob, D.J., Heterogeneous chemistry and tropospheric ozone, Atmos. Environ., 34, 2131-2159, 2000.

Jaeglé, L., Quinn, P. K., Bates, T. S., Alexander, B., and Lin, J.-T.: Global distribution of sea salt aerosols: new constraints from in situ and remote sensing observations, Atmos. Chem. Phys., 11, 3137-3157, doi:10.5194/acp-11-3137-2011, 2011.

Jones, A.E., Anderson, P.S., Begoin, M., Brough, N., Hutterli, M.A., Marshall, G.J., Richter, A., Roscoe, H.K. and Wolff, E.W.: BrO, blizzards, and drivers of polar tropospheric ozone depletion events. Atmospheric Chemistry and Physics, 9(14), pp.4639-4652, 2009.

Jourdain, B., Preunkert, S., Cerri, O., Castebrunet, H., Udisti, R., and Legrand, M.: Year-round record of size segregated aerosol composition in central Antarctica (Concordia station): Implications for the degree of fractionation of sea-salt particles, J. Geo-phys. Res., 113, D14308, doi:10.1029/2007JD009584, 2008.

Kaleschke, L., Richter, A., Burrows, J., Afe, O., Heygster, G., Notholt, J., Rankin, A. M., Roscoe, H. K., Hollwedel, J., Wagner, T., and Jacobi, H.-W.: Frost flowers on sea ice as a source of sea salt and their influence on tropospheric halogen chemistry, Geophys. Res. Lett., 31, L16114, doi:10.1029/2004GL020655, 2004.

Kalnajs, L. E. and Avallone, L. M.: Frost flower influence on springtime boundary-layer ozone depletion events and at- mospheric bromine levels, Geophys. Res. Lett., 33, L10810, doi:10.1029/2006GL025809, 2006.

Klimont, Z., Kupiainen, K., Heyes, C., Purohit, P., Cofala, J., Rafaj, P., Borken-Kleefeld, J., and Schöpp, W.: Global anthropogenic emissions of particulate matter including black carbon, Atmos. Chem. Phys., 17, 8681–8723, doi:10.5194/acp-17-8681-2017, 2017.

Koo, J.-H., Wang, Y., Kurosu, T. P., Chance, K., Rozanov, A., Richter, A., Oltmans, S. J., Thompson, A. M., Hair, J. W., Fenn, M. A., Weinheimer, A. J., Ryerson, T. B., Solberg, S., Huey, L. G., Liao, J., Dibb, J. E., Neuman, J. A., Nowak, J. B., Pierce, R. B., Natarajan, M., and Al-Saadi, J.: Characteristics of tropospheric ozone depletion events in the Arctic spring: analysis of the ARCTAS, ARCPAC, and ARCIONS measurements and satellite BrO observations, Atmos. Chem. Phys., 12, 9909-9922, https://doi.org/10.5194/acp-12-9909-2012, 2012.

Krnavek, L., Simpson, W. R., Carlson, D., Dominé, F., Douglas, T. A., and Sturm, M.: The chemical composition of surface snow in the Arctic: examining marine, terrestrial, and

atmospheric influence, Atmos. Environ., 50, 349–359, doi:10.1016/j.atmosenv.2011.11.033, 2012.

Kwok, R., and D. Rothrock: Decline in Arctic sea ice thickness from submarine and ICESat records: 1958–2008, Geophys. Res. Lett., 36, L15501, doi:10.1029/2009GL039035, 2009.

Kwok, R. and Cunningham, G.F.: Variability of Arctic sea ice thickness and volume from CryoSat-2. Phil. Trans. R. Soc. A, 373(2045), p.20140157, 2015.

Levelt, P.F., van den Oord, G.H., Dobber, M.R., Malkki, A., Visser, H., de Vries, J., Stammes, P., Lundell, J.O. and Saari, H. The ozone monitoring instrument. IEEE Transactions on geoscience and remote sensing, 44(5), pp.1093-1101, 2006.

Lewis, E. R. and Schwartz, S. E.: Sea Salt Aerosol Production: Mechanisms, Methods, Measurements, and Models: A Critical Review, American Geophysical Union, Washington, D.C., 2004.

Lewis, E. R. and Schwartz, S. E.: Comment on "size distribution of sea-salt emissions as a function of relative humidity", Atmos. Environ., 40, 588–590, 2006.

Li, C., Hsu, N. C., Sayer, A. M., Krotkov, N. A., Fu, J. S., Lamsal, L. N., Lee, J., and Tsay, S.-C.: Satellite observation of pollutant emissions from gas flaring activities near the Arctic, Atmos. Environ., 133, 1–11, doi:10.1016/j.atmosenv.2016.03.019, 2016.

Li, M., Zhang, Q., Kurokawa, J.-I., Woo, J.-H., He, K., Lu, Z., Ohara, T., Song, Y., Streets, D. G., Carmichael, G. R., Cheng, Y., Hong, C., Huo, H., Jiang, X., Kang, S., Liu, F., Su, H., and Zheng, B.: MIX: a mosaic Asian anthropogenic emission inventory under the international collaboration framework of the MICS-Asia and HTAP, Atmos. Chem. Phys., 17, 935-963, doi:10.5194/acp-17-935-2017, 2017.

Liao, J., Huey, L. G., Tanner, D. J., Flocke, F. M., Orlando, J. J., Neuman, J. A., Nowak, J. B., Weinheimer, A. J., Hall, S. R., Smith, J. N., Fried, A., Staebler, R. M., Wang, Y., Koo, J.-H., Cantrell, C. A., Weibring, P., Walega, J., Knapp, D. J., Shepson, P. B., and Stephens, C. R.: Observations of inorganic bromine (HOBr, BrO, and Br2) speciation at Bar- row, Alaska, in spring 2009, J. Geophys. Res., 117, D00R16, doi:10.1029/2011JD016641, 2012.

Lin, S.-J., and R.B. Rood: Multidimensional flux form semi-Lagrangian transport schemes, Mon. Wea. Rev., 124, 2046-2070, 1996.

Lin, J.-T., and M. McElroy, Impacts of boundary layer mixing on pollutant vertical profiles in the lower troposphere: Implications to satellite remote sensing, Atmospheric Environment, 44(14), 1726-1739, doi:10.1016/j.atmosenv.2010.02.009, 2010.

Liu, H., Jacob, D. J., Bey, I., and Yantosca, R. M.: Constraints from 210Pb and 7Be on wet deposition and transport in a global three- dimensional chemical tracer model driven by assimilated meteorological fields, J. Geophys. Res., 106(D11), 12 109–12 128, 2001.

Liu, Z. Y., Vaughan, M., Winker, D., Kittaka, C., Getzewich, B., Kuehn, R., Omar, A., Powell, K., Trepte, C., and Hostetler, C.: The CALIPSO Lidar Cloud and Aerosol Discrimination: Version 2 Algorithm and Initial Assessment of Performance, J. Atmos. Ocean. Tech., 26, 1198–1213, doi:10.1175/2009JTECHA1229.1, 2009.

Mann, G. W., Anderson, P. S., and Mobbs, S. D.: Profile measurements of blowing snow at Halley, Antarctica, J. Geophys. Res., 105, 24,491–24,508, 2000.

Mao, J., Jacob, D. J., Evans, M. J., Olson, J. R., Ren, X., Brune, W. H., Clair, J. M. St., Crounse, J. D., Spencer, K. M., Beaver, M. R., Wennberg, P. O., Cubison, M. J., Jimenez, J. L., Fried, A., Weibring, P., Walega, J. G., Hall, S. R., Weinheimer, A. J., Cohen, R. C., Chen, G., Crawford, J. H., McNaughton, C., Clarke, A. D., Jaeglé, L., Fisher, J. A., Yantosca, R.

M., Le Sager, P., and Carouge, C.: Chemistry of hydrogen oxide radicals (HOx) in the Arctic troposphere in spring, Atmos. Chem. Phys., 10, 5823-5838, doi:10.5194/acp-10-5823-2010, 2010.

Mao, J., S. Fan, D.J. Jacob, K.R. Travis, Radical loss in the atmosphere from Cu-Fe redox coupling in aerosols, Atmos. Chem. Phys, 13,509-519, 2013.

Martin, R.V., D.J. Jacob, R.M. Yantosca, Mian Chin, and Paul Ginoux, Global and Regional Decreases in Tropospheric Oxidants from Photochemical Effects of Aerosols, J. Geophys. Res., 108(D3), 4097, doi:10.1029/2002JD002622, 2003.

Morin, S., Marion, G. M., von Glasow, R., Voisin, D., Bouchez, J., and Savarino, J.: Precipitation of salts in freezing seawater and ozone depletion events: a status report, Atmos. Chem. Phys., 8, 7317-7324, https://doi.org/10.5194/acp-8-7317-2008, 2008.

Maslanik, J. A., Fowler. C., Stroeve, J., Drobot, S., Zwally, H. J., Yi, D., Emery, W.J.: A younger, thinner ice cover: increased potential for rapid, extensive ice loss. Geophys. Res. Lett. 34: L24501. doi:10.1029/2007GL032043, 2007.

Massom, R. A., Eicken, H., Hass, C., Jeffries, M. O., Drinkwater, M. R., Sturm, M., Worby, A. P., Wu, X., Lytle, V. I., Ushio, S., Morris, K., Reid, P. A., Warren, S. G., and Alli- son, I.: Snow on Antarctic sea ice, Rev. Geophys., 39, 413–445, doi:10.1029/2000RG000085, 2001.

May, N. W., Quinn, P. K., McNamara, S. M., and Pratt, K. A.: Multiyear study of the dependence of sea salt aerosol on wind speed and sea ice conditions in the coastal Arctic, J. Geophys. Res. Atmos., 121, 9208–9219, doi:10.1002/2016JD025273, 2016.

Mundy, C.J., Barber, D.G. and Michel, C.: Variability of snow and ice thermal, physical and optical properties pertinent to sea ice algae biomass during spring, J. Mar. Syst., 58, 107–120, doi:10.1016/j.jmarsys.2005.07.003, 2005.

Nandan, V., Geldsetzer, T., Yackel, J., Mahmud, M., Scharien, R., Howell, S., King, J., Ricker, R. and Else, B.: Effect of Snow Salinity on CryoSat-2 Arctic First-Year Sea Ice Freeboard Measurements, Geophys. Res. Lett., 44(20), doi:10.1002/2017GL074506, 2017.

Munro, R., Eisinger, M., Anderson, C., Callies, J., Corpaccioli, E., Lang, R., Lefebvre, A., Livschitz, Y. and Albinana, A.P.: GOME-2 on MetOp. In Proc. of The 2006 EUMETSAT Meteorological Satellite Conference, Helsinki, Finland (Vol. 1216, p. 48), 2006.

Nakawo, M. and Sinha, N.K.: Growth rate and salinity profile of first-year sea ice in the high Arctic. J. Glaciol, 27(96), pp.315-330, doi: DOI: 10.1017/ S0022143000015409, 1981.

Neuman, J. A., Nowak, J. B., Huey, L. G., Burkholder, J. B., Dibb, J. E., Holloway, J. S., et al. (2010). Bromine measurements in ozone depleted air over the Arctic Ocean. Atmospheric Chemistry and Physics, 10(14), 6503–6514. https://doi.org/10.5194/acp-10-6503-2010.

Nilsson, E. D., Rannik, U., Swietlicki, E., Leck, C., Aalto, P. P., Zhou, J., and Norman, M.: Turbulent aerosol fluxes over the Arc- tic Ocean 2, Wind-driven sources from the sea, J. Geophys. Res., 106, 32111–32124, 2001.

Olivier, J. G. J. and Berdowski, J. J. M.: Global emissions sources and sinks, in: The Climate System, Berdowski, J., Guicherit, R. and B. J. Heij (eds.), A.A. Balkema Publishers/Swets & Zeitlinger Publishers, Lisse, The Netherlands, ISBN 90 5809 255 0, 33-78, 2001.

Oltmans, S.J. and Komhyr, W.D. Surface ozone distributions and variations from 1973–1984: Measurements at the NOAA Geophysical Monitoring for Climatic Change Baseline

Observatories. Journal of Geophysical Research: Atmospheres, 91(D4), pp.5229-5236, 1986.

Oltmans, S. J., Johnson, B. J., and Harris, J. M.: Springtime bound- ary layer ozone depletion at Barrow, Alaska: Meteorological in- fluence, year-to-year variation, and long-term change, J. Geo- phys. Res. Atmos., 117, D00R18, doi:10.1029/2011JD016889, 2012.

Oum, K. W.: Formation of Molecular Chlorine from the Photolysis of Ozone and Aqueous Sea-Salt Particles, Science, 279, 74–76, doi:10.1126/science.279.5347.74, 1998.

Parrella, J.P., Jacob, D.J., Liang, Q., Zhang, Y., Mickley, L.J., Miller, B., Evans, M.J., Yang, X., Pyle, J.A., Theys, N. and Roozendael, M.V.: Tropospheric bromine chemistry: implications for present and pre-industrial ozone and mercury. Atmospheric Chemistry and Physics, 12(15), pp.6723-6740, 2012.

Peterson, P. K., Poehler, D., Sihler, H., Zielcke, J., General, S., Friess, U., et al. (2017). Observations of bromine monoxide transport in the Arctic sustained on aerosol particles. Atmospheric Chemistry and Physics, 17(12), 7567–7579. https://doi.org/10.5194/acp-17-7567-2017

Pratt, K.A., Custard, K.D., Shepson, P.B., Douglas, T.A., Pöhler, D., General, S., Zielcke, J., Simpson, W.R., Platt, U., Tanner, D.J. and Huey, L.G.: Photochemical production of molecular bromine in Arctic surface snowpacks. Nature Geoscience, 6(5), pp.351-356, 2013.

Rankin, A.M., Auld, V. and Wolff, E.W.: Frost flowers as a source of fractionated sea salt aerosol in the polar regions. Geophysical Research Letters, 27(21), pp.3469-3472, 2002.

Renner, A.H., Gerland, S., Haas, C., Spreen, G., Beckers, J.F., Hansen, E., Nicolaus, M. and Goodwin, H.: Evidence of Arctic sea ice thinning from direct observations. Geo. Res. Lett., 41(14), pp.5029-5036, doi:10.1002/2014GL060369, 2014.

Reynolds, R. W., Rayner, N. A., Smith, T. M., Stokes, D. C., and Wang, W.: An improved in situ and satellite SST analysis for climate, J. Clim., 15, 1609–1625, doi:10.1175/1520-0442(2002)015<1609:AIISAS>2.0.CO;2, 2002.

Rienecker, M. M., Suarez, M. J., Gelaro, R., Todling, R., Bacmeister, J., Liu, E., Bosilovich, M. G., Schubert, S. D., Takacs, L., Kim, G.-K., Bloom, S., Junye, C., Collins, D., Conaty, A., da Silva, A., Gu, W., Joiner, J., Koster, R. D., Lucchesi, R., Molod, A., Owens, T., Pawson, S., Pegion, P., Redder, C. R., Reichle, R., Robertson, F. R., Ruddick, A. G., Sienkiewicz, M., and Woollen, J.: MERRA: NASA's modern-era retrospective analysis for research and applications, J. Climate, 24, 3624–3648,doi:10.1175/JCLI-D-11-00015.1, 2011.

Roscoe, H. K., Brooks, B., Jackson, A. V., Smith, M. H., Walker, S. J., Obbard, R. W., and Wolff, E. W.: Frost flowers in the laboratory: Growth, characteristics, aerosol, and the underlying sea ice, J. Geophys. Res., 116, D12301, doi:10.1029/2010JD015144, 2011.

Sander, R., Keene, W.C., Pszenny, A.A.P., Arimoto, R., Ayers, G.P., Baboukas, E., Cainey, J.M., Crutzen, P.J., Duce, R.A., Hönninger, G. and Huebert, B.J.: Inorganic bromine in the marine boundary layer: a critical review. Atmospheric Chemistry and Physics, 3(5), pp.1301-1336, 2003.

Salawitch, R. J., Canty, T. P., Kurosu, T. P., Chance, K., Liang, Q., da Silva, A., Pawson, S., Nielsen, J. E., Rodriguez, J. M., Bhar- tia, P. K., Liu, X., Huey, L. G., Liao, J., Stickel, R. E., Tanner, D., Dibb, J. E., Simpson, W. R., Donohoue, D., Weinheimer, A. J., Flock, F. M., Knapp, D. J., Dmontzka, D. D., Neuman, J., Nowak, J. B., Ryerson, T. B., Oltmans, S.,

Blake, D. R., Atlas, E. L., Kinnison, D. E., Tilmes, S., Pan, L., Hendrick, F., Van Roozendael, M., Kreher, K., Johnston, P. V., Gao, R. S., Bui, T. P., Chen, G., Pierce, R., Crawford, J. H., and Jacob, D. J.: A new interpretation of total column BrO during Arctic spring, Geophys. Res. Lett., 37, L21805, doi:10.1029/2010GL043798, 2010.

Schmidt, J.A., Jacob, D.J., Horowitz, H.M., Hu, L., Sherwen, T., Evans, M.J., Liang, Q., Suleiman, R.M., Oram, D.E., Le Breton, M. and Percival, C.J.: Modeling the observed tropospheric BrO background: Importance of multiphase chemistry and implications for ozone, OH, and mercury. Journal of Geophysical Research: Atmospheres, 121(19), 2016.

Schroeder, W. H., Anlauf, K. G., Barrie, L. A., Lu, J. Y., Steffen, A., Schneeberger, D. R., and Berg, T.: Arctic springtime depletion of mercury, Nature, 394, 331–332, doi:10.1038/28530, 1998.

Seguin, A.M., Norman, A.L. and Barrie, L.: Evidence of sea ice source in aerosol sulfate loading and size distribution in the Canadian High Arctic from isotopic analysis, J. Geophys. Res. Atmos., 119, 1087–1096, doi:10.1002/2013JD020461, 2014.

Seibert, P. and Frank, A.: Source-receptor matrix calculation with a Lagrangian particle dispersion model in backward mode, Atmos. Chem. Phys., 4, 51-63, doi:10.5194/acp-4-51-2004, 2004.

Shaw, P. M., Russell, L. M., Jefferson, A., and Quinn, P. K.: Arctic organic aerosol measurements show particles from mixed combustion in spring haze and from frost flowers in winter, Geophys. Res. Lett., 37, L10803, doi:10.1029/2010GL042831, 2010.

Sherwen, T., Evans, M. J., Carpenter, L. J., Andrews, S. J., Lid- ster, R. T., Dix, B., Koenig, T. K., Sinreich, R., Ortega, I., Volkamer, R., Saiz-Lopez, A., Prados-Roman, C., Mahajan, A. S., and Ordóñez, C.: Iodine's impact on tropospheric oxidants: a global model study in

GEOS-Chem, Atmos. Chem. Phys., 16, 1161– 1186, doi:10.5194/acp-16-1161-2016, 2016a.

Sherwen, T., Schmidt, J. A., Evans, M. J., Carpenter, L. J., Großmann, K., Eastham, S. D., Jacob, D. J., Dix, B., Koenig, T. K., Sinreich, R., Ortega, I., Volkamer, R., Saiz-Lopez, A., Prados- Roman, C., Mahajan, A. S., and Ordóñez, C.: Global impacts of tropospheric halogens (Cl, Br, I) on oxidants and composition in GEOS-Chem, Atmos. Chem. Phys., 16, 12239–12271, doi:10.5194/acp-16-12239-2016, 2016b.

Simpson, W. R., von Glasow, R., Riedel, K., Anderson, P., Ariya, P., Bottenheim, J., Burrows, J., Carpenter, L. J., Frieß, U., Goodsite, M. E., Heard, D., Hutterli, M., Jacobi, H.-W., Kaleschke, L., Neff, B., Plane, J., Platt, U., Richter, A., Roscoe, H., Sander, R., Shepson, P., Sodeau, J., Steffen, A., Wagner, T., and Wolff, E.: Halogens and their role in polar boundary-layer ozone depletion, Atmos. Chem. Phys., 7, 4375-4418, doi:.5194/acp-7-4375-2007, 2007a.

Simpson, W. R., Carlson, D., Hönninger, G., Douglas, T. A., Sturm, M., Perovich, D., and Platt, U.: First-year sea-ice contact predicts bromine monoxide (BrO) levels at Barrow, Alaska better than potential frost flower contact, Atmos. Chem. Phys., 7, 621-627, doi:10.5194/acp-7-621-2007, 2007b.

Simpson, W. R., Peterson, P. K., Frieß, U., Sihler, H., Lampel, J., Platt, U., Moore, C., Pratt, K., Shepson, P., Halfacre, J., and Nghiem, S. V.: Horizontal and vertical structure of reactive bromine events probed by bromine monoxide MAX-DOAS, Atmos. Chem. Phys., 17, 9291-9309, https://doi.org/10.5194/acp-17-9291-2017, 2017.

Slinn, S.A. and Slinn, W.G.N.: Predictions for particle deposition on natural waters. Atmospheric Environment (1967), 14(9), pp.1013-1016, 1980.

Stammerjohn, S., Massom, R., Rind, D. and Martinson, D.: Regions of rapid sea ice change: An inter - hemispheric seasonal comparison. Geo. Res. Lett., 39(6), doi:10.1029/2012GL050874, 2012.

Steffen, A., Douglas, T., Amyot, M., Ariya, P., Aspmo, K., Berg, T., Bottenheim, J., Brooks, S., Cobbett, F., Dastoor, A., Dommergue, A., Ebinghaus, R., Ferrari, C., Gardfeldt, K., Goodsite, M. E., Lean, D., Poulain, A. J., Scherz, C., Skov, H., Sommar, J., and Temme, C.: A synthesis of atmospheric mercury depletion event chemistry in the atmosphere and snow, Atmos. Chem. Phys., 8, 1445-1482, doi:10.5194/acp-8-1445-2008, 2008.

Stohl, A., Hittenberger, M., and Wotawa, G.: Validation of the Lagrangian particle dispersion model FLEXPART against large scale tracer experiment data, Atmos. Environ., 32, 4245–4264, doi:10.1016/S1352-2310(98)00184-8, 1998.

Stohl, A., Forster, C., Frank, A., Seibert, P., and Wotawa, G.: Technical note: The Lagrangian particle dispersion model FLEXPART version 6.2, Atmos. Chem. Phys., 5, 2461-2474, doi:10.5194/acp-5-2461-2005, 2005.

Tarasick, D. W. and Bottenheim, J. W.: Surface ozone depletion episodes in the Arctic and Antarctic from historical ozonesonde records, Atmos. Chem. Phys., 2, 197–205, doi:10.5194/acp-2- 197-2002, 2002.

Theys, N., Van Roozendael, M., Hendrick, F., Yang, X., De Smedt, I., Richter, A., Begoin, M., Errera, Q., Johnston, P.V., Kreher, K. and De Mazière, M.: Global observations of tropospheric BrO columns using GOME-2 satellite data. Atmospheric Chemistry and Physics, 11(4), p.1791, 2011.

Thompson, C. R., Shepson, P. B., Liao, J., Huey, L. G., Apel, E. C., Cantrell, C. A., et al. (2015). Interactions of bromine, chlorine, and iodine photochemistry during ozone depletions in

Barrow, Alaska. Atmospheric Chemistry and Physics, 15(16), 9651–9679. https://doi.org/10.5194/acp-15-9651-2015.

Travis, K. R., D. J. Jacob, J. A. Fisher, P. S. Kim, E. A. Marais, L. Zhu, K. Yu, C. C. Miller, R. M. Yantosca, M. P. Sulprizio, A. M. Thompson, P. O. Wennberg, J. D. Crounse, J. M. St. Clair, R. C. Cohen, J. L. Laughner, J. E. Dibb, S. R. Hall, K. Ullmann, G. M. Wolfe, J. A. Neuman, and X. Zhou, Why do models overestimate surface ozone in the Southeast United States, Atmos. Chem. Phys., 16, 13561-13577, doi:10.5194/acp-16-13561-2016, 2016.

Turner, J., Comiso, J.C., Marshall, G.J., Lachlan‐Cope, T.A., Bracegirdle, T., Maksym, T., Meredith, M.P., Wang, Z. and Orr, A.: Non‐annular atmospheric circulation change induced by stratospheric ozone depletion and its role in the recent increase of Antarctic sea ice extent. Geo., Res. Lett., 36(8), doi:10.1029/2009GL037524, 2009.

Obbard, R. W., Roscoe, H.K., Wolff, E. W., and Atkinson, H. M.: Frost flower surface area and chemistry as a function of salinity and temperature, J. Geophys. Res., 114, D20305, doi:10.1029/2009JD012481, 2009.

Olivier, J. G. J. and Berdowski, J. J. M.: Global emissions sources and sinks, in: The Climate System, Berdowski, J., Guicherit, R. and B. J. Heij (eds.), A.A. Balkema Publishers/Swets & Zeitlinger Publishers, Lisse, The Netherlands, ISBN 90 5809 255 0, 33-78, 2001.

Omar, A. H, Winker, D. M., Kittaka, C., Vaughan, M. A., Liu, Z. Y., Hu, Y. X., Trepte, C. R., Rogers, R. R., Ferrare, R. A., Lee, K. P., Kuehn, R. E., and Hostetler, C. A.: The CALIPSO automated aerosol classification and lidar ratio se- lection algorithm, J. Atmos. Ocean. Technol., 26, 1994–2014, doi:10.1175/2009JTECHA1231.1, 2009.

Palm, S. P., Yang, Y. K., Spinhirne, J. D., and Marshak, A.: Satellite remote sensing of blowing snow proper- ties over Antarctica, J. Geophys. Res.-Atmos., 116, 1–16, doi:10.1029/2011jd015828, 2011.

Palm, S. P., Kayetha, V., Yang, Y., and Pauly, R.: Blowing snow sublimation and transport over Antarctica from 11 years of CALIPSO observations, The Cryosphere, 11, 2555-2569, doi:10.5194/tc-11-2555-2017, 2017.

Parkinson, C. L. and Cavalieri, D. J.: Antarctic sea ice variability and trends, 1979–2010, The Cryosphere, 6, 871-880, doi:10.5194/tc-6-871-2012, 2012.

Perovich, D. K. and Richter-Menge, J. A.: Surface characteristics of lead ice, J. Geophys. Res., 99, 16341–16350, doi:10.1029/94JC01194, 1994.

Pye, H. O. T., Liao, H., Wu, S., Mickley, L. J., Jacob, D. J., Henze, D. K., and Seinfeld, J. H.: Effect of changes in cli- mate and emissions on future sulfate-nitrate-ammonium aerosol levels in the United States, J. Geophys. Res., 114, D01205, doi:10.1029/2008JD010701, 2009.

Udisti, R., Dayan, U., Becagli, S., Busetto, M., Frosini, D., Legrand, M., Lucarelli, F., Preunkert, S., Severi, M., Traversi, R., and Vitale, V.: Sea spray aerosol in central Antarctica. Present atmospheric behaviour and implications for paleoclimatic reconstructions, Atmos. Environ., 52, 109–120, doi:10.1016/j.atmosenv.2011.10.018, 2012.

van der Werf, G. R., Randerson, J. T., Giglio, L., Collatz, G. J., Mu, M., Kasibhatla, P. S., Morton, D. C., DeFries, R. S., Jin, Y., and van Leeuwen, T. T.: Global fire emissions and the contribution of deforestation, savanna, forest, agricultural, and peat fires (1997–2009), Atmos. Chem. Phys., 10, 11707-11735, doi:10.5194/acp-10-11707-2010, 2010.

van Donkelaar, A., Martin, R. V., Leaitch, W. R., Macdonald, A. M., Walker, T. W., Streets, D. G., Zhang, Q., Dunlea, E. J., Jimenez, J. L., Dibb, J. E., Huey, L. G., Weber, R., and Andreae, M. O.: Analysis of aircraft and satellite measurements from the Intercontinental Chemical Transport Experiment (INTEX-B) to quantify long-range transport of East Asian sulfur to Canada, Atmos. Chem. Phys., 8, 2999-3014, doi:10.5194/acp-8-2999-2008, 2008.

Wagenbach, D., Ducroz, F., Mulvaney, R., Keck, L., Minikin, A., Legrand, M., Hall, J. S., and Wolff, E. W.: Sea-salt aerosol in coastal Antarctic regions, J. Geophys. Res., 103, 10 961–10 974, doi:10.1029/97JD01804, 1998.

Wagner, T., Leue, C., Wenig, M., Pfeilsticker, K. and Platt, U.: Spatial and temporal distribution of enhanced boundary layer BrO concentrations measured by the GOME instrument aboard ERS-2. Journal of geophysical research, 106, p.24, 2001.

Wang, Y., D.J. Jacob, and J.A. Logan, Global simulation of tropospheric O3-NOx-hydrocarbon chemistry, 1. Model formulation, J. Geophys. Res., 103, D9,10,713-10,726, 1998.

Wang, Q., Jacob, D. J., Fisher, J. A., Mao, J., Leibensperger, E. M., Carouge, C. C., Le Sager, P., Kondo, Y., Jimenez, J. L., Cubison, M. J., and Doherty, S. J.: Sources of carbonaceous aerosols and deposited black carbon in the Arctic in winter-spring: implications for radiative forcing, Atmos. Chem. Phys., 11, 12453-12473, doi:10.5194/acp-11-12453-2011, 2011.

Warren, S. G., Rigor, I. G., Untersteiner, N., Radionov, V. F., Bryazgin, N. N., Aleksandrov, Ye. I., and Colony, R.: Snow depth on Arctic sea ice, J. Climate, 12, 1814–1829, 1999.

Weeks, W. F., and Lee O. S.: Observations on the physical properties of sea-ice at Hopedale, Labrador, Arctic, 11(3), 135–155, doi: 10.14430/arctic3740, 1958.

Weeks, W. F. and Ackley, S. F.: The growth, structure and properties of sea ice, 9–164, Plenum Press, New York, 1986.

Weller, R., Woltjen, J., Piel, C., Resenberg, R., Wagenbach, D., Konig-Langlo, G., and Kriews, M.: Seasonal variability of crustal and marine trace elements in the aerosol at Neumayer station, Antarctica, Tellus, 60, 742–752, doi:10.1111/j.1600-0889.2008.00372.x, 2008.

Wesely, M. L., Parameterization of surface resistance to gaseous dry deposition in regional-scale numerical models, Atmos. Environ., 23, 1293-1304, 1989.

Winker, D. M., Vaughan, M. A., Omar, A., Hu, Y., and Powell, J. A.: Overview of the CALIPSO Mission and CALIOP Data Processing Algorithms, J. Atmos. Ocean. Tech., 26, 2310–2323, doi:10.1175/2009JTECHA1281.1, 2009.

Winker, D. M., Tackett, J. L., Getzewich, B. J., Liu, Z., Vaughan, M. A., and Rogers, R. R.: The global 3-D distribution of tropospheric aerosols as characterized by CALIOP, Atmos. Chem. Phys., 13, 3345-3361, doi:10.5194/acp-13-3345-2013, 2013.

Winker, D.: CALIPSO LID L2 Standard HDF File -Version 4.10. NASA Langley Research Center Atmospheric Science Data Center DAAC. https://doi.org/10.5067/CALIOP/CALIPSO/LID_L2_05kmAPro-Standard-V4-10, Last Access February 2018, 2016

Wolff, E. W., Fischer, H., Fundel, F., Ruth, U., Twarloh, B., Littot, G. C., Mulvaney, R., Rothlisberger, R., de Angelis, M., Boutron, C. F., Hansson, M., Jonsell, U., Hutterli, M. A., Bigler, M., Lambeck, K., Kaufmann, P., Stauffer, B., Stocker, T. F., Steffensen, J. P., Siggaard-Andersen, M. L., Udisti, R., Becagli, S., Castellano, E., Severi, M., Wagenbach, D., Barbante, C., Gabrielli, P., and Gaspari, V.: Southern Ocean sea-ice extent, productivity

and iron flux over the past eight glacial cycles, Nature, 440, 491–496, doi:10.1038/nature04614, 2006.

Worby, A.P., Massom, R.A., Allison, I., Lytle, V.I. and Heil, P.: East Antarctic sea ice: A review of its structure, properties and drift. Antarctic sea ice: physical processes, interactions and variability, pp.41-67, 1998.

Xu, L., Russell, L. M., Somerville, R. C. J., and Quinn, P. K.: Frost flower aerosol effects on Arctic wintertime longwave cloud radiative forcing, J. Geophys. Res.-Atmos., 118, 13282–13291, doi:10.1002/2013JD020554, 2013.

Xu, J.-W., Martin, R. V., Morrow, A., Sharma, S., Huang, L., Leaitch, W. R., Burkart, J., Schulz, H., Zanatta, M., Willis, M. D., Henze, D. K., Lee, C. J., Herber, A. B., and Abbatt, J. P. D.: Source attribution of Arctic black carbon constrained by aircraft and surface measurements, Atmos. Chem. Phys., 17, 11971-11989, doi:10.5194/acp-17-11971-2017, 2017.

Yang, X., Pyle, J. A., and Cox, R. A.: Sea salt aerosol production and bromine release: Role of snow on sea ice, Geophys. Res. Lett., 35, L16815, doi:10.1029/2008GL034536, 2008.

Yang, X., Pyle, J. A., Cox, R. A., Theys, N., and Van Roozendael, M.: Snow-sourced bromine and its implications for polar tropospheric ozone, Atmos. Chem. Phys., 10, 7763-7773, doi:10.5194/acp-10-7763-2010, 2010.

Yang, X., Neděla, V., Runštuk, J., Ondrušková, G., Krausko, J., Vetráková, Ľ., and Heger, D.: Evaporating brine from frost flowers with electron microscopy and implications for atmospheric chemistry and sea-salt aerosol formation, Atmos. Chem. Phys., 17, 6291-6303, doi:10.5194/acp-17-6291-2017, 2017.

Zender, C.S., Bian, H. and Newman, D. Mineral Dust Entrainment and Deposition (DEAD) model: Description and 1990s dust climatology. Journal of Geophysical Research: Atmospheres, 108(D14), 2003.

Zhang, L., Gong, S., Padro, J., and Barrie, L.: A size-segregated particle dry deposition scheme for an atmospheric aerosol module, Atmos. Environ., 35, 549–560, 2001.